The composite ~~radar-GNSS~~ radar and GNSS spectrum of auroral plasma turbulence

Magnus F Ivarsen[1,2], Kaili Song[3], Luca Spogli[4], Jean-Pierre St-Maurice[1,5], Devin R Huyghebaert[6,1], Brian Pitzel[1], Saif Marei[1], Yangyang Shen[7], Satoshi Kasahara[8], Kunihiro Keika[8], Yoshizumi Miyoshi[9], Tomo Hori[9], Atsuki Shinbori[9], Kazuhiro Yamamoto[9], David R Themens[10], P. T. Jayachandran[3], Yoichi Kazama[11], Shiang-Yu Wang[11], Ayako Matsuoka[12], Iku Shinohara[13], Takefumi Mitani[13], Takeshi Takashima[13], Shoichiro Yokota[14], Yoshiya Kasahara[15], and Glenn C Hussey[1]

[1]Department of Physics and Engineering Physics, University of Saskatchewan, Saskatoon, Canada
[2]The European Space Agency Centre for Earth Observation, Frascati, Italy
[3]Physics Department, University of New Brunswick, Fredericton, Canada
[4]Istituto Nazionale di Geofisica e Vulcanologia, Rome, Italy
[5]Department of Physics and Astronomy, University of Western Ontario, London, Canada
[6]Leibniz Institute of Atmospheric Physics, Kühlungsborn, Germany
[7]Department of Physics, University of Alberta, Edmonton, Canada
[8]Department of Earth and Planetary Science, University of Tokyo, Tokyo, Japan
[9]Institute for Space-Earth Environmental Research, Nagoya University, Nagoya, Japan
[10]School of Engineering, University of Birmingham, Birmingham, UK
[11]Academia Sinica Institute of Astronomy and Astrophysics, Taipei, Taiwan
[12]Data Analysis Center for Geomagnetism and Space Magnetism, Kyoto University, Kyoto, Japan
[13]Institute of Space and Astronautical Science, Japan Aerospace Exploration Agency, Sagamihara, Japan
[14]Department of Earth and Space Science, Osaka University, Toyonaka, Japan
[15]Graduate School of Natural Science and Technology, Kanazawa University, Kanazawa, Japan

Abstract. In the auroral ionosphere, plasma turbulence acts as an important dissipation mechanism for magnetospheric energy and as the primary cause of radio wave scintillation. Characterizing ~~auroral plasma~~ this turbulence across its full spatial extent has historically been limited by the narrow bandwidths of individual instruments. ~~Our investigation approaches the problem of obtaining accurate, scale-dependent information using the physics of the Farley-Buneman (FB) instability, a modified two-stream plasma instability.~~ In this study, we construct a composite spatial powerspectrum of plasma turbulence in the auroral electrojets spanning roughly four orders of magnitude in scale (from ~ 100 km down to ~ 20 m). This is achieved by combining a recent Monte-Carlo-based method of spatial clustering of very-high-frequency (VHF) radar echoes, with phase screen information derived from global navigation satellite system (GNSS) signals, using ground-based instrumentation in Canada. ~~Through multi-instrument conjunctions with the European Swarm and Japanese Arase missions, we observe that the clustering of electrojet turbulence matches the structuring of field-aligned currents, and correlates with magnetospheric electron fluxes. Statistical analysis of the *composite* spectra , as well as a very large database of radar clustering spectra only, reveals a consistently steep~~ Both measurements yield the two-dimensional spectral density of the turbulent irregularity field, and the two spectra agree closely across their shared band between 750 m and 3000 m. Across ten radar and GNSS conjunction events, the composite spectra exhibit a steady, scale-free decay of spectral power~~in the auroral electrojets, with the most probable~~

~~spectral index being near $-8/3$. The observations suggest a continuous, scale-invariant cascade that frequently preserves the spatial signature of its magnetospheric drivers, where we outline a way for Alfvén waves to structure the turbulent E-region. Furthermore, we demonstrate that the plasma structures guilty of causing GPS scintillations (~~, with overall spectral indices of mean -2.50 and standard deviation 0.24 in that two-dimensional convention, consistently interrupted by spectral knees near 5 km and near 270 m. We further compare three independent velocity measurements in the same volume: radar Doppler velocities, tracked radar target motions, and GNSS phase screen drifts. The ~ 270 ~~meters in size) were moving~~ meter structures responsible for GPS scintillation moved at the ion acoustic speed, ~~implying that those structures were, in fact, FB waves, and we thereby establish an observational basis for low-frequency electrojet turbulence.~~ near 500 m/s, well below the concurrent $\mathbf{E} \times \mathbf{B}$ drifts near 1000 m/s traced by the target motions, a velocity signature consistent with long-wavelength Farley-Buneman (FB) waves, complementing the 3 m FB waves the radar observes directly. Conjunctions with the Japanese Arase mission show that spectral steepening correlates with precipitating magnetospheric electron flux, while conjunctions with the European Swarm mission confirm that the radar target motions track the F-region plasma drift. The method that we present, the composite ~~radar-GNSS spectra, will on both counts~~ radar and GNSS spectra, may offer useful empirical constraints for future efforts seeking to simulate the "sub-grid" turbulence that complicates the magnetosphere-ionosphere coupling around aurorae.

1 Introduction

In Earth's upper atmosphere, at the lower edge of the partially ionized layers of the ionosphere, intense plasma turbulence is observed during geomagnetic storms, in the form of crashing waves that appear inside the electrical currents of the auroral electrojets. Here, collisions between charged particles and neutral molecules become so frequent that the ratio of collision to cyclotron frequency is sufficiently large to demagnetize ions below 120 km, and demagnetize electrons below 80 km. The resulting difference in charge carrier mobility between 80 and 120 km allows strong electric fields in the aurora to drive Hall currents at times. For plasma drifts below around 400 m/s, the electrical currents remain laminar, but, when the electron drift speed exceeds the ion acoustic speed, C_s, the laminar current becomes unstable to electrostatic density fluctuations, triggering the Farley-Buneman (FB) instability through the ion inertia excited by the motion of the irregularities, which is driven by the electron plasma ($\mathbf{E} \times \mathbf{B}$) drift (Farley, 1963; Buneman, 1963).

Inside turbulent regions of the ionosphere, regions that can be several hundred kilometers in size, small-scale fluctuations in plasma density can disrupt traversing satellite navigation (GNSS) signals (Kintner P. M. et al., 2007; Jin et al., 2014), ultimately caused by the presence around aurorae of intense, broad-spectrum, electrostatic turbulence (Sato, 1972; Sudan and Keskinen, 1977; Fejer and Kelley, 1980; Keskinen, 1981; Huba et al., 1985). While plasma turbulence modulates radio signal phase and amplitude in ways that are detrimental to human technological progress (Moen et al., 2013), it also produces the 'radio aurora' ~~(Hultqvist and Egeland, 1964; ?)~~(Hultqvist and Egeland, 1964; Sahr and Fejer, 1996), the clear signature of aurorae, shown *solely* through the plasma turbulence that they create.

The problem of understanding this turbulence is therefore directly related to its effect on radio signals: what starts out as large-wavelength (ultra-low frequency, or ULF) waves generated by the solar wind at the bow shock or magnetopause of Earth

(Krämer et al., 2024; Ivarsen et al., 2025c), will eventually produce the ~ 300 meter-size waves that disrupt GNSS signals (Song et al., 2023). This inherent and essentially non-linear coupling between the largest and smallest scales in geospace exacerbates the problem. The scale-dependent problem is tackled by turbulence physics, and its nature is typically inspected through application of Fourier analysis.

By elucidating the amount of fluctuation power in each individual wavenumber (or wavevector), Fourier analysis, in its many forms, can produce a *spectrum,* the power spectral density (PSD), and the shape of this spectrum is an expression of the scale-dependent physics that governs the overall turbulent cascade from the largest unstable magnetohydrodynamic (MHD) modes, to the small-scale kinetic plasma turbulence in Earth's upper atmosphere, that we described at the onset of this Introduction.

In this paper, we present an observational model of the spectrum $P(k)$ of plasma turbulence in the auroral ionosphere, and this method spans almost four orders in magnitude in wavenumber k, with equivalent scale-sizes from 100 km down to around 20 m. We do this by combining two recent, novel methods of PSD estimation: a spatial spectrum based on Monte-Carlo-simulations (Ivarsen et al., 2023a), and a temporal Fourier analysis of GNSS phase fluctuations (Song et al., 2025). The former correlates the spatial positions of very-high frequency (VHF) coherent radar echoes from the turbulent electrojets on scale-sizes between ~ 100 km and ~ 500 m, while the latter translates a temporal Fourier spectrum of GPS signals received from the ground, to a spatial spectrum via phase screen theory, for scale-sizes between $\sim$5 km to ~ 20 m.

We analyze the characteristics of the composite ~~radar-GNSS~~ radar and GNSS spectrum around diffuse auroras~~and find that the composite spectrum of plasma turbulence matches signatures in the field-aligned currents (FAC) inside the aurorae, consistent with recent discoveries,~~ , and we find that ~~spectral steepness~~ the spectral index correlates with observations of particle precipitation from the magnetosphere. ~~Surprisingly, we observe that the composite spectrum of plasma turbulence near aurorae seem *universally steep*, and *dissipative*, with spectral indices that only approach inertial values on scale-sizes that are limited.~~ The composite spectra near aurorae are close to scale-free across the observed range, with two reproducible break points interrupting an otherwise continuous decay of spectral power.

In what follows, in Section 2 we shall describe the two methods, and provide some details on spectral density interpretation in ionospheric physics. We then present in Section 3 results from 10 case studies, including conjunction studies with orbiting satellites, as well as statistical results from ~~four~~ two years of radar data. In Section 4, we discuss the implications of our results, where we argue that the detailed description of these spectra provide unique opportunities for fluid MHD models to parameterize and verify the turbulent cascade that culminates in plasma turbulence smaller than those models can resolve.

2 Methodology

This section is a summary of recent papers of a highly technical nature, pertaining to coherent radar data from Ionospheric Continuous-wave E-region Bistatic Experimental Auroral Radar (ICEBEAR) (Ivarsen et al., 2023a) and GPS signal analysis from the Canadian High-Arctic Ionospheric Network (CHAIN) (Jayachandran et al., 2009; Song et al., 2025). At the end of this section, we comment on current interpretations of spectral density measurements in the auroral ionosphere.

2.1 Pairwise VHF radar echo clustering

We analyze coherent scatter radar data from ICEBEAR, an experimental radar capable of imaging the distribution of small-scale plasma turbulence in 3-dimensions (3D), (Huyghebaert et al., 2019; Lozinsky et al., 2022) yielding the ICEBEAR 3D dataset. The radar's 6 m wavelength yields a 3 m Bragg wavelength, meaning we observe meter-scale turbulent waves. The turbulence echoes are seen towards the northern horizon in Saskatchewan, Canada.

ICEBEAR can record thousands of echo locations per second, yielding exceedingly large point-cloud datasets, (Ivarsen et al., 2023c, 2024c) and we are in this paper segmenting the radar data in 6 second bins. The radar echoes observed inside each bin are clustered using `dbscan` following Ivarsen et al. (2024c).

Ivarsen et al. (2023a) developed a method to correlate the pairwise spatial positions of each imaginable pair of echoes found inside such radar echo point-clouds, using the *two-point correlation function,* $\xi(r)$,

$$n^2[1+\xi(r)] = \langle \rho(x)\rho(x+r)\rangle, \tag{1}$$

where n is the average number density of echoes in a given volume, and $\rho(x)$ is the number density of echoes at location x, and r is a distance away from x, and in Figure 2c) we show $\xi(r)$ calculated for the cluster shown in Figure 2b). The method yields spatial power spectra $P(k)$ through a Hankel transform, (Ivarsen et al., 2016; Baddour, 2011)

$$P(k) = \int_0^\infty \xi(r) J_0(kr)\, r dr, \tag{2}$$

where $J_0(kr)$ are zeroth order Bessel functions of the first kind. Such power spectra yield spectral information roughly between the scale-sizes 750 m and $\sim 10^5$ m, much larger than the ICEBEAR radar wavelength (3 m). Later, the spectra were demonstrated to match the small-scale structuring of field-aligned electrical currents associated with pulsating aurorae (Ivarsen et al., 2024a) as well as F-region plasma structuring. (Ivarsen et al., 2023b)

2.2 E-region target radar motions

To complement pairwise echo clustering, we exploit the recent discovery that a 3D coherent radar such as ICEBEAR can be operated as a target radar, by identifying and tracking coherent clusters of radar echoes through time and space (Ivarsen et al., 2024c). The method , which was tested against actual displays, relies on an unsupervised machine learning algorithm to automatically identify dense clusters of radar echoes, before it quantifies the spatial trajectories of such clusters. This yields the actual $\mathbf{E}\times\mathbf{B}$ motion of the source regions, which have to be the same as the F-region plasma velocities normally observed just in the F region (Ivarsen et al., 2024c, d, 2025c). This method overcomes the well-known fact that coherent E-region radars normally observe structures moving close to, or below, the ion acoustic speed of the turbulent auroral E-region owing to the nonlinear properties of large amplitude Farley-Buneman waves observed by coherent E-region radars (e.g., Fejer and Kelley, 1980; Sahr and Fejer, 1996). It has been clearly shown that the difference between the two velocities can be considerable under strong electric field conditions [e.g., Figure 2 in Foster and Erickson (2000), and references therein].

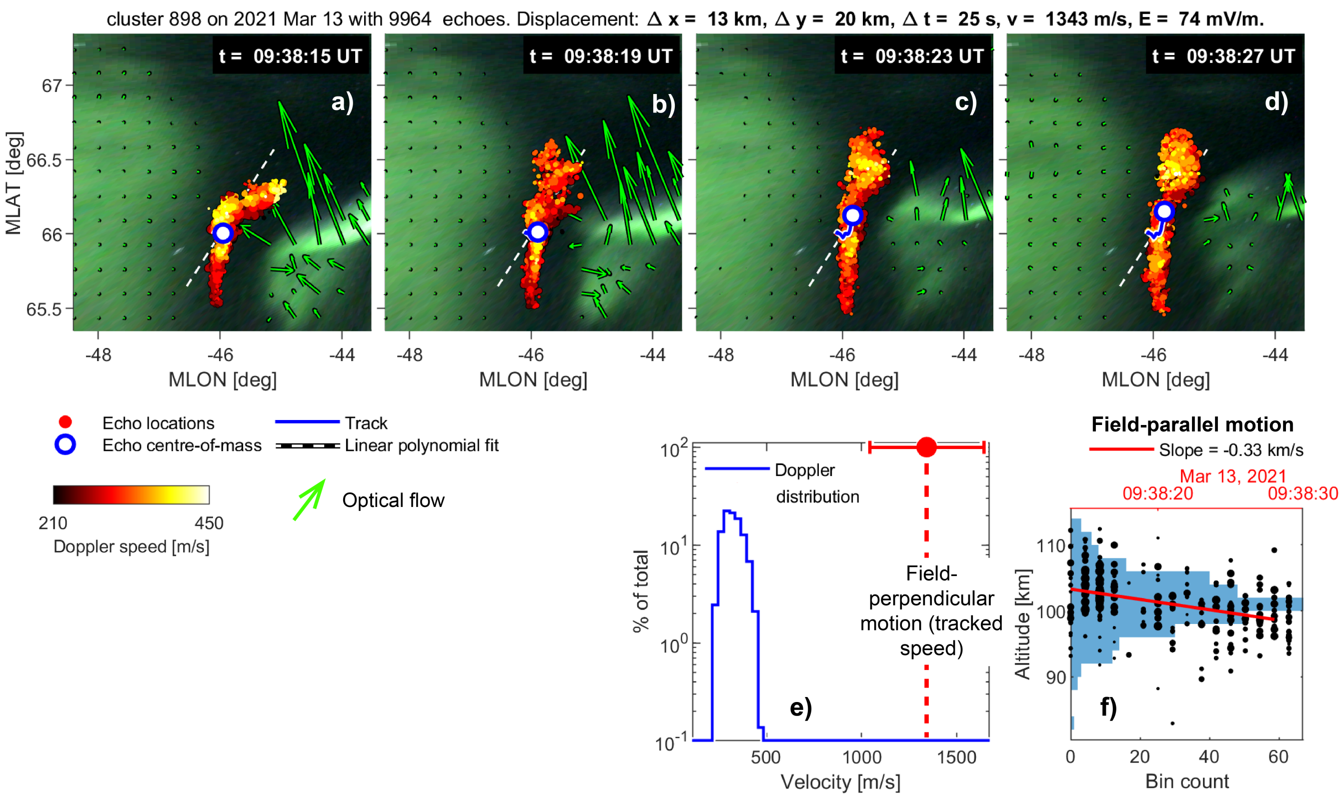

Figure 1. ~~Panels a–d): Identifying & tracking a cluster of VHF radar echoes,~~ **Panels a) to d): Identifying & tracking a cluster of VHF radar echoes,** emanating from Farley-Buneman turbulence between two auroral forms. Echo point-clouds are color-coded by Doppler speed, and superposed on optical aurora images using the TREx RGB (Gillies et al., 2020) camera located at Rabbit Lake, with green arrows showing the Horn-Schunk method of optical flow vectors ~~Barron et al. (1994)~~(Barron et al., 1994), applied to the green channel of the auroral images [see Ivarsen et al. (2024d) for details of such conjunction studies]. **Panel e)** contrasts the Doppler speeds with the tracked, target motion, while **Panel f)** shows the altitude distribution of this cluster, with the echo altitude cloud in a scatterplot (top, red axis).

In Figure 1 we present a typical example, tracked ICEBEAR echo cluster, superposed on auroral imaging by TREx (RGB, 2023). The cluster's *centre-of-mass,* or median echo location, moved around 24 kilometers in the magnetic north-east direction, tracked for a 25-second duration. That yields a target motion of some 1300 m/s, and these target motions, really the translatory displacement of echo centres-of-mass, have been demonstrated to track the wider ionospheric "frozen-in" drift (Ivarsen et al., 2024c, d, 2025c). In Figure 1, the 1300 m/s tracked motion, much faster than the ~ 350 m/s speed obtained from the radar echo Doppler shifts, corresponds to a 74 mV/m electric field. We note that a unique feature in the analysis of echo cluster 898 (Figure 1) is the fact that we have tracked this cluster as it *descended* slightly, moving downward with a speed of 330 m/s; the first instance of quantifying the vertical descent of a coherent plasma structure in the auroral E-region.

2.3 GPS phase fluctuations and the phase-screen drifts

To complement tracking and radar spectral analysis of echo locations, we perform a time-series analysis of GPS amplitude and phase fluctuations measured with the Ionospheric Scintillation Monitor Receiver (ISMR) located at the Rabbit Lake research station (58.23°N, 256.32°E), which is part of the Canadian High Arctic Ionospheric Network (CHAIN Jayachandran et al., 2009). The ISMR in Rabbit Lake is a Septentrio PolaRxS, (Bougard et al., 2011) capable of recording the raw phase and post-correlation in-phase (I) and quadrature (Q) samples of GNSS signals at a 100 Hz sampling rate. For the purposes of our work, we concentrate solely on GPS.

The signals emitted by GPS satellites and subsequently recorded by the ISMR are disrupted by plasma irregularities linked with instabilities and resultant turbulent phenomena in the ionospheric plasma, (Yeh and Liu, 1982; Kintner P. M. et al., 2007). This introduces stochastic fluctuations in the recorded signal amplitude (McCaffrey and Jayachandran, 2019; Spogli et al., 2021; Ghobadi et al., 2020; Song et al., 2023; Meziane et al., 2023) . We derive a spatial k-spectrum from the temporal fluctuations in the recorded signal in the Rabbit Lake ISMR (directly beneath the radar field-of-view) using phase screen theory (Yeh and Liu, 1982) . In this framework, the Fresnel frequency f_F is derived from the second zero-crossing of the normalized cross-spectrum of the L1-L2 or L1-L5 carrier frequencies, (Song et al., 2025) or, equivalently, the prominent breakpoint or "knee" in the ionosphere-free linear combination (IFLC) spectrum, ~~(Song et al., 2025)~~(Song et al., 2025; Meziane et al., 2025) , shown with a blue line in Figure 2d). We then estimate the average drift velocity $\mathbf{v}_d$ of the irregular structures in the region where they originate (Forte and Radicella, 2002; Spogli et al., 2021) , using $v_d = f_F \lambda_F$, where λ_F is the corrected Fresnel scale (Ghidoni et al., 2025),

$$\lambda_F = \frac{\sqrt{2\lambda_{\mathrm{GPS}} h}}{\sin^{3/2}\theta}, \tag{3}$$

where $\lambda_{\mathrm{GPS}} \approx$ 20 cm is the wavelength of the GPS signal, θ is the GPS satellite elevation angle, and h is the altitude of the irregularity layer, here assumed to be around $h = 105$ km (see Appendix ~~C~~ B for a sensitivity analysis of this assumption). The expression for λ_F takes into account the oblique incidence observational geometry, for which the distance between the antenna and the irregularity layer becomes $h \sin\theta$. We estimate the irregularity velocity under the approximation of a single, thin ~~layer~~phase screen: all phase perturbation is assigned to one layer at altitude h. While we account for the azimuthal dependence introduced by the elliptical projection of the scan path under anisotropic conditions (Teunissen and Montenbruck, 2017), we do not apply an axial ratio correction to the Fresnel scale λ_F itself, effectively treating the base irregularities as isotropic. The velocity measured with this method yields an estimate of the relative velocity between the satellite pierce-point and the ionospheric irregularities, often referred to as "scan velocity" ~~. (Yeh and Liu, 1982)~~(Yeh and Liu, 1982). The thin-layer approximation, the assumed layer altitude, the isotropy approximation, and the motion of the pierce point itself all enter the inferred velocity, and each is bounded quantitatively in Appendix B.

We construct a spectrum based on the IFLC spectrum (for scale-sizes smaller than the Fresnel scale), and a spectrum of Total Electron Content (TEC) fluctuations for scale-sizes larger than that threshold. The result is a k-spectrum that yields spectral information on scales roughly between 5 km and $\sim$ 20 m (the red spectrum in Figure 2d), which is readily compared to the spectrum of "echo clustering" of co-located irregular structures seen by radar.

The two spectra, one from radar and one from GNSS, are then simply spliced (see Figure A1 in the Appendix A): the two spectra feature an overlapping transition zone spanning spatial scales roughly between 750 m and 3000 m. To avoid artifacts from spectral leakage, we truncate the radar spectrum for scales smaller than 750 m, and the GNSS spectrum for scales larger than 3000 m. Within this overlapping regime, the spectral shapes from the two independent methods match strikingly well.

The events analyzed in this study were selected in two stages. We first identified 49 one-hour intervals of strong ICEBEAR echo activity, without reference to any GNSS data. Within those intervals, we then searched for GPS pierce points that overlapped the radar echo regions in time and space while exhibiting amplitude scintillation, which yielded the 10 conjunction events analyzed below. Amplitude fluctuations are a prerequisite of the phase screen method: without them, neither the Fresnel frequency nor the IFLC spectrum is defined, and no composite spectrum can be constructed. The sample of composite spectra is therefore conditioned on scintillation-producing events by construction, and we weigh the consequences of this conditioning against a radar-only, scintillation-independent climatology in Section 3.

In addition to spectral inferences, the GPS-derived scan velocity could readily be compared to both the radar Doppler and target velocities. As discussed above, the target velocities reveal the true $\boldsymbol{E} \times \boldsymbol{B}$-drift, while the Doppler shifts normally should not exceed an ion-acoustic speed of about 400 to 450 m/s if they come from near 100 km altitude. As it turned out, for a strong electric field event that we studied in detail, the observed GPS scan velocities were highly consistent with the upper limit of the Doppler shift E region radar observations found at the ion-acoustic speed near 100 km altitude (see Figures 4 and 8 below). Those speeds were, in turn, far smaller than the bulk of the target speeds in the region. The ~~most plausible interpretation of this unexpected~~ interpretation most consistent with this result is that the 270 m structures associated with the Fresnel zone near 105 km were themselves nonlinear Farley-Buneman waves~~. This is the only explanation we could think of for their motion at the ion-acoustic speed. Indeed, there~~ ; we develop this argument, and weigh it against alternatives, in Section 4.1. There is no law to state that Farley-Buneman waves cannot exist at 270 m, although the growth rate from ion inertia~~l~~ has to exceed that from the gradient-drift instability. This would only be expected for very strong electric fields (or for geometries in which the ambient density gradients are perpendicular to the ambient electric field, which is not very likely).

2.4 Spectral density interpretation

The result from combining the two methods of spectral density measurements described in the foregoing section is presented in Figure 2e), in the form of the *composite ~~radar-GNSS~~ radar and GNSS spectrum*, the primary observable analyzed in the present study. The clustering spectrum is seamlessly consistent with the TEC spectrum. Prominent breakpoints are seen at spatial scales 4.6 km and 262 m, and the inferred spectral index (see Eq. 4) is similar for the largest (> 50 km) and smallest (< 100 m) scale-sizes. What follows ~~is a reflection on the role of such spectral density measurements in ionospheric plasma~~specifies the physical quantity the composite spectrum represents, the spectral convention it obeys, and the procedure used to extract indices and break points.

In studies of space plasma turbulence, one expects spectral densities to adhere to a simple power law if not for the full wavenumber range, at least for substantial wavenumber intervals (Phelps and Sagalyn, 1976; Tsunoda, 1988; Spicher et al.,

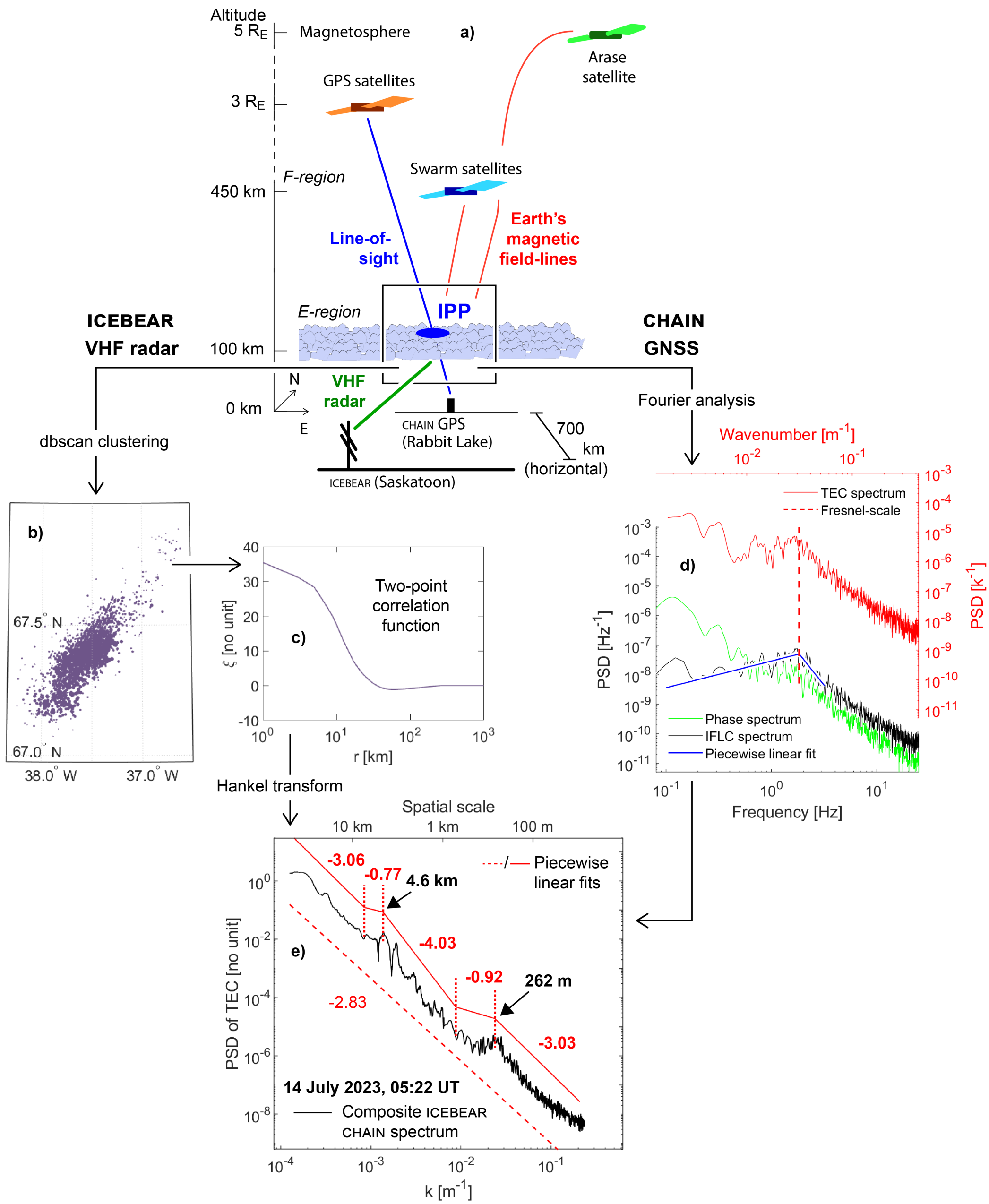

Figure 2. Panel a) shows a schematic overview of the observational space, with the various instruments, and the measurement geometry, annotated. Panel b) shows a sample 6-second radar point-cloud cluster, while **Panel c)** shows the two-point correlation function based on that point-cloud (Eq. 1). **Panel d)** shows example phase (green), IFLC (black), and TEC (red) spectra, with a piecewise linear fit shown with a blue line, and with the Fresnel scale (wavenumber) shown with a red, dashed line, based on measurements performed in the two-minute interval starting at 05:21 UT on 14 July 2023. **Panel e)** shows the resulting composite ~~radar–GNSS~~ radar and GNSS spectrum for that interval, where the two-point correlation function of all nearby echo clusters have been Hankel-transformed to yield an average clustering spectrum. A five-component piecewise linear fit (solid red line) and a single linear fit (dashed red line) are shown above and below the spectrum respectively, with spectral indices posted in red.

2014), meaning that the spectra are categorized with equations of the type

$$P(k) \propto k^{-\alpha}, \tag{4}$$

where $P(k)$ is the power spectral density, k denotes wavenumber ($k = 2\pi/L$, L being spatial scale), and α is a positive constant describing the decay in spectral power with decreasing spatial scale (increasing k) (Sudan et al., 1973; Mounir et al., 1991; Ivarsen et al., 2021). α is referred to as the spectral index and is a central quantity of measurement in the present study. As just stated above, in the auroral region of Earth's ionosphere, the steady decay in power indicated by Eq. (4) needs to often be broken into segments, with typical 'break-points' occurring on spatial scales between 1 km – and 5 km (Villain et al., 1986; Ivarsen et al., 2024e, 2023b) and between 30 m – and 300 m (Basu et al., 1990; Mounir et al., 1991; Spicher et al., 2014; Hamza et al., 2023), in clear agreement with Figure 2e).

The two data sources obey a common spectral convention, which we now make explicit. The Hankel transform in Eq. (2) inverts the two-point correlation function of a two-dimensional field, and therefore returns the *two-dimensional spectral density*, a quantity defined per unit area d^2k in the wavenumber plane. A one-dimensional cut through the same field carries a spectral index that is shallower by exactly one power of k; a measured two-dimensional index of $-8/3$ corresponds, for example, to a one-dimensional index of $-5/3$ (see Ivarsen et al., 2026).

The GNSS-derived spectra carry the same convention. In the weak-scatter phase screen approximation, the signal phase is the line-of-sight integral of the density fluctuation, and by the projection-slice theorem the areal spectrum of the phase field is proportional to the transverse cut of the density spectrum, a cut that preserves the transverse spectral index. The measured temporal spectrum is then a one-dimensional scan of that phase field along the pierce-point track, involving a single marginalization (integration) over transverse wavenumber, whereas a hypothetical one-dimensional in-situ measurement of the same field involves two. The GNSS phase and TEC spectra therefore exhibit one power of k above one-dimensional spectra of the same medium, which places them on the same footing as the radar clustering spectra. The Fresnel filter imprints the knee and oscillations near the Fresnel scale, and leaves the asymptotic slope unchanged, and so this footing holds on both sides of the Fresnel scale; the predicted oscillatory ripple below the Fresnel scale is present in the measured spectra. A full treatment of these reductions is given in the supplementary methods of Ivarsen et al. (2026). The shared convention is confirmed empirically by the seamless agreement between the radar and GNSS spectra across the 750 m to 3000 m band. All spectral indices quoted in this paper are two-dimensional indices: published one-dimensional indices, whether from in-situ slices or along-track spacecraft spectra, differ by one power of k and are not directly comparable, whereas break-point positions are unaffected by the convention.

Spectral indices and break points are extracted with an automatic slope and break-point detection algorithm based on piecewise linear Hermite polynomials [the shape language modeling framework of D'Errico (2009)], with applications to ionospheric spectra described in Ivarsen et al. (2019) and Ivarsen et al. (2021). Each spectrum is fitted in log-log space with a small number of free knots: the knot positions return the break points, and the segment gradients return the spectral indices. Composite spectra are fitted with a five-segment model, and, in parallel, with a single linear fit whose gradient serves as the overall index quoted throughout. Power amplitudes are normalized between instruments to facilitate direct shape comparison.

Break-points are often thought of as transition markers between inertial and fully collisional regimes in the F region (Keskinen and Huba, 1990; Kivanc and Heelis, 1998), or they can be viewed as “injection wavelengths" if the break points go through a peak. The injection wavelengths or the knees and the various spectral indices, or slopes, and relative magnitudes, are all, in the end, indicative of various scale-dependent instability processes that contribute to the structuring of the plasma (Sudan et al., 1973; Mounir et al., 1991).

~~Another view posits that measured spectral density is produced by the dimensionality constraints that are placed on the system, in which the emergence of ordered dissipative structures are as much a *consequence* and a *source* of chaos, (Marov and Kolesnichen and where spectral shape is dictated by *self-organized criticality*, (Marek and Schreiber, 2022) from which all the structure of the universe can presumptively be deduced.~~

3 Results

We shall start by presenting two ground-ground conjunctions between the VHF radar ICEBEAR and a CHAIN GPS receiver at Rabbit Lake. The first event (Figure 3) revolves around a relatively brief, two-minute conjunction, and the second event (Figure 4) details an extended one-hour conjunction.

The first, Figure 3a), exhibits a number of radar echo clusters being tracked, seen moving past a GPS ionospheric pierce-point (IPP), with a north-eastern bearing. Figure 3c, d) detail the strong temporal correlation ($\rho = 0.94$) between the rate of detected echoes and the GPS amplitude fluctuations. Panel e) shows the composite spectrum, with detailed log-log linear fits of the two spectra shown with black, red, and blue dashed lines. We observe the clear tendency for the two instruments to essentially measure the very same structure from two different perspectives. Both the temporal (Figure 3c, d) and spatial (Figure 3e) components agree remarkably well, confirming a clear common and immediate origin of the two multi-scale signals.

Next, we shall dissect an extended, one-hour conjunction, during which we observed three GPS amplitude scintillation events [implying small-scale structuring (Song et al., 2023)]. Figure 4 shows the detailed observations made by ICEBEAR and CHAIN, during which ICEBEAR detected and localized a staggering 2.3 million individual radar echoes (see Figure A1~~a–c~~ a) to c) for the three composite ~~radar-GNSS~~ radar and GNSS spectra calculated during this event).

Figure 4a) shows an overview of the observational volume, the ionospheric E-region, during the 20-minute interval 08:~~45–09~~45 to 09:05 UT, with the tracked ICEBEAR echo cluster motions shown with arrows demonstrating the fast and dynamic appearance of radar aurorae; the tracked echo motions~~– the result of~~ , obtained by treating ICEBEAR as a tracking radar rather than a Doppler radar~~–~~ , move through a GPS pierce point denoted with a green circle. The next panels in Figure 4 details the velocity observations made by the two instruments during the full one-hour interval. Panel b) shows clearly that while the GPS phase drifts match the observed radar Doppler speeds in an excellent fashion (average ~ 500 m/s), the observed target motions greatly exceed those speeds (average ~ 1000 m/s). This is caused by the fact that the radar echoes’ source regions being associated with precipitation patterns (aurorae), move with the $\mathbf{E} \times \mathbf{B}$ drift of the F-region plasma (Ivarsen et al., 2024c, d, 2025b). However, the Doppler speeds (and, very clearly also the GPS phase drifts) are limited to the ion acoustic speed, usually ~~400-600~~400 to

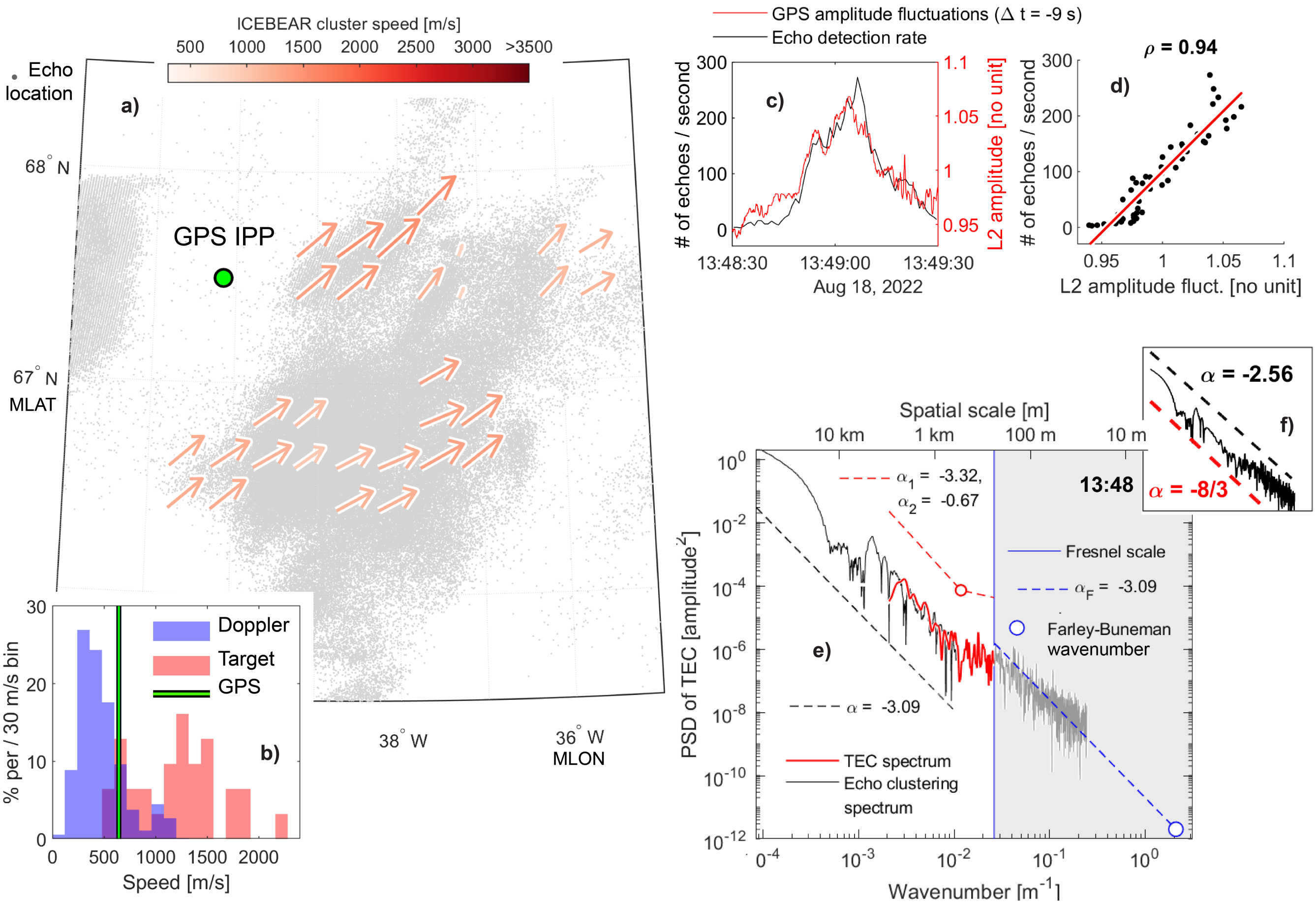

Figure 3. Panel a) shows the spatially averaged vector field of ICEBEAR target motions detected during the 15-minute interval starting on 13:45 UT on 18 August 2022, gray dots indicate echo locations, color-coded arrows denote the target motions, while a green circle indicates the position of a GPS pierce-point (IPP). **Panel b)** shows histograms for the Doppler speeds (blue) and echo cluster speeds (red), compared to the GPS phase screen velocity (green line). The next three panels detail a brief, two-minute conjunction event between ICEBEAR and CHAIN, with **Panel c)** showing the observed GPS amplitude fluctuations (red, right axis) with radar echo detection rates superposed (black), where we have applied a nine-second lag to align the two timeseries. **Panel d)** shows this data in a scatterplot, with Pearson correlation coefficient indicated, exhibiting a very strong correlation (Pearson coefficient $\rho = 0.94$). ~~**Panel f)**~~ **Panel e)** shows the composite ~~radar-GNSS~~ radar and GNSS spectrum, with spectral index calculations indicated. ~~Inset **Panel f)**~~ An inset in **Panel e)** shows the overall spectral index fitted to the composite spectrum (black dashed line), compared to a ~~theoretical kinetic Alfvén value~~ reference slope of -8/3 (red dashed line).

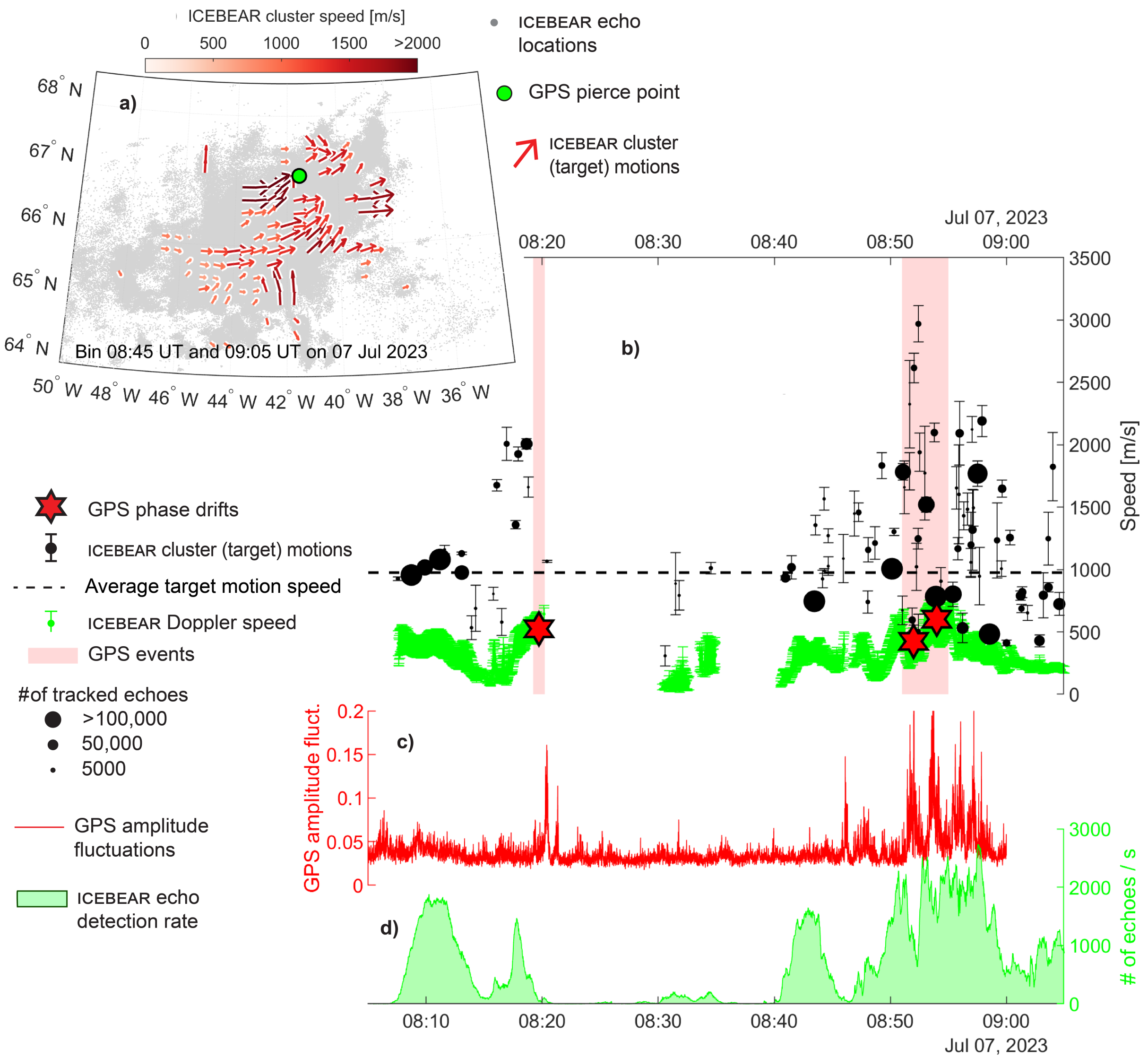

Figure 4. An extended conjunction between ICEBEAR and the CHAIN GPS receiver at Rabbit Lake in Saskatchewan, Canada, on 7 July 2023. Panel a) shows geospace over Rabbit Lake in geomagnetic coordinates, with the locations of 1.4 million radar echoes shown with grey dots, using the altitude-adjusted corrected geomagnetic coordinate system. Color- and size-coded arrows show the spatial average of the observed ICEBEAR cluster motions in the interval between 08:45 UT and 09:05 UT, while the location of the GPS pierce point is shown with a green circle (100 km altitude). **Panel b)** shows, for the one-hour interval between 08:05 UT and 09:05 UT, a timeseries of binned ICEBEAR echo cluster speeds (black, size-coded circles, with errorbars), ICEBEAR Doppler speeds (green dots with errorbars), and GPS phase drift speeds (red hexagrams). A black dashed line shows the average cluster speed. **Panel c)** shows fluctuation in recorded GPS signal amplitude (red axis), while **Panel d)** shows the rate of detected ICEBEAR echoes (green axis).

600 m/s (Foster and Erickson, 2000; Oppenheim and Dimant, 2013; Chau and St.-Maurice, 2016)(Foster and Erickson, 2000; Oppenheim

.

We were able to substantiate the foregoing using conjugate observations by the European Space Agency's Swarm satellites (Friis-Christensen et al., 2006; Wood et al., 2022), a constellation that is in a polar orbit around Earth (inclination 87°, altitude $\sim 450 - 500$~450 to 500 km). Figure 5a) details a triple-conjunction between ICEBEAR, CHAIN, and two Swarm satellites. The latter orbited through a region of active radar echo detection, and we observe that the radar echo cluster speeds agree very well with the F-region ion drift speeds observed by Swarm A, in accordance with earlier conjunctions as well as statistical comparisons (Ivarsen et al., 2024c, d). In addition, Figure 5b) shows that these speeds are clearly greater than the GPS phase drifts observed at the pierce point, repeating the velocity separation seen in the ground-based comparisons above.

A triple conjunction between ICEBEAR, CHAIN and Swarm A, during a period more limited than that of Figure ?? Panel a) shows locations in geospace whereas panels b) and c) show the composite radar-GNSS spectrum. See Figure ?? in the Appendix A.

Following Ivarsen et al. (2023a) and Ivarsen et al. (2024a), we next Fourier analyze the Swarm 50 Hz magnetic field fluctuations transformed into a mean-field-aligned coordinate system, yielding information on the field-aligned current structuring, or, alternatively, current filamentation (Park et al., 2017; Ivarsen et al., 2020). The quantity is analogous to the structuring of magnetic field-tubes in the plane perpendicular to the geomagnetic field. As the satellites orbit through the topside (F-region) ionosphere with a velocity of $v_s = 7.62$ km/s, we apply Taylor's "frozen-in" assumption (Fredricks and Coroniti, 1976) to convert the temporal FAC powerspectra to spatial k-spectra. These are superposed on the composite radar-GNSS spectra in The composite radar and GNSS spectrum for this conjunction is shown in Figure 5c), showing good agreement on a wide range of spatial scales between 10^5 m and 750 m (below 750 m, the Swarm spectra drop off, indicating an *effective* Nyquist frequency of 12.5 Hz for the Swarm magnetic field instrument). See Section ?? in the Appendix for details of this triple conjunction.

We normalize the power amplitude between the various instruments to facilitate a direct spectral shape comparison, and we apply an automatic spectral slope- & break-point detection algorithm based on piecewise linear Hermite polynomials (D'Errico, 2009), with details described in, e.g., Ivarsen et al. (2019) and Ivarsen et al. (2021). For the overlapping scale-sizes between 750 m and 3000 m, the spectral shapes are observed to match surprisingly well. The exponent of the fitted power laws, referred to as spectral index, tracks energy dissipation (Ivarsen et al., 2019), and we observe in Figure 5c) that the shape-wise agreement between the F-region FAC spectrum and the E-region radar-GNSS is excellent, echoing recent conjunctions of a similar nature (Ivarsen et al., 2023a, b, 2024a), and consistent with the filamentary nature of the field-aligned currents observed around diffuse aurorae (Gillies et al., 2015).

Meanwhile, using a Swarm-based electromagnetic wave impedance analysis due to Pakhotin et al. (2018), Figure 5d–g) demonstrates a clear Alfvénic signature at Swarm altitude. We deduce this from the, at times, strong (> 0.9) correlation in the transverse E-M components (Figure 5f) and , d), with the , at times, flat impedance spectra (Figure 5g). We therefore ascertain that Alfvén waves were actively threading the flux tubes connected to the E-region radar echoes. Seen together with ***(i)*** the overall spectral indices in Figure 5c) being close to the kinetic-Alfvén value of -8/3 (Boldyrev and Perez, 2012; David and Galtier, 2019), and ***(ii)*** the spectral shape of the composite radar-GNSS spectrum matches filaments in the aurorae very well (Figure 5c), we

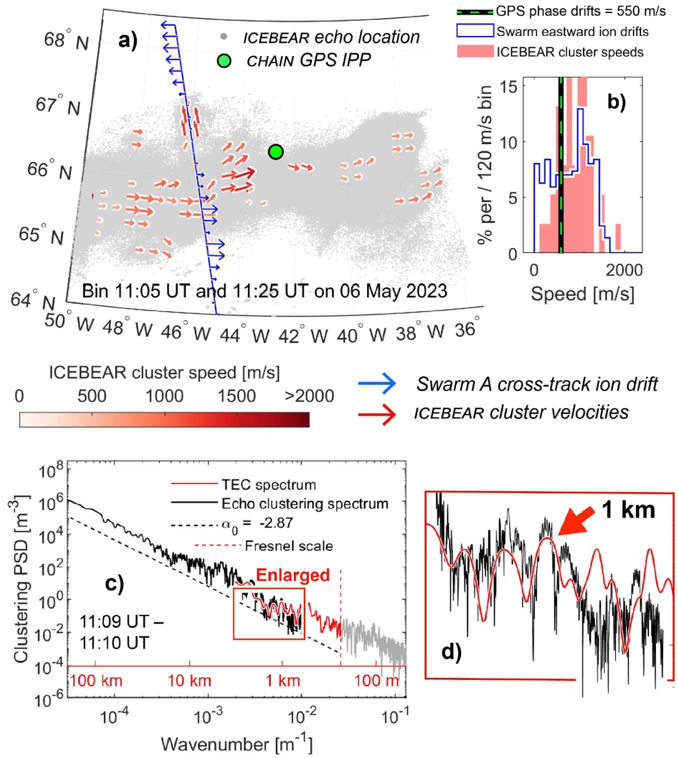

Figure 5. Panel a) shows the spatial distribution of radar echoes (grey point-cloud), the ICEBEAR echo cluster velocities (red arrows), the Swarm A cross-track ion velocities (blue arrows), and the ionospheric GNSS pierce point (green circle). **Panel b)** shows the observed GPS phase drift speed (black and green line), and distributions of the Swarm A cross-track ion drift magnitudes (blue line) and observed ICEBEAR echo cluster (target) motions (red shaded area). **Panel c)** shows the ~~average~~ composite radar and GNSS spectrum~~for the five-minute interval starting at 11:06 UT on 6 May 2023 (Black line). The normalized spectrum of eastward magnetic fluctuations measured by Swarm C is shown~~ , with a ~~green line. A five-component piecewise log-log~~ linear fit ~~is shown above the spectra (solid red line) while a single-slope fit is shown below the spectrum (dashed red line). Spectral indices~~ and ~~breakpoints are~~ spectral index indicated~~in red and black lettering respectively. Panel d) superposes the meridional electric field component (black) with the eastward magnetic residual (red, right axis), panel e)~~ ; **panel d)** shows ~~the observed difference in magnetic residual field by Swarm A and C (shifted using~~ a ~~cross-correlation analysis), and panels f) and g) show~~ close-up of the ~~Pearson correlation and an impedance spectrogram respectively, both within running 16-s windows, and the latter in accordance with the decoherence masking method due to Pakhotin et al. (2018)~~former. ~~See Figure **??** in the Appendix for additional details.~~

~~point to the likely Alfvénic origin for the echo point-cloud shapes.~~ five-segment piecewise fit and the overall index indicated. The event exhibits the same organization as the conjunctions presented above: a continuous, near scale-free decay across the resolved range, interrupted by break points near 5 km and near the Fresnel scale.

Note that the observations reported in the present paper were performed during arctic summer, and were thus occurring in full daylight, except for the Figure 1 example. As such, we have no *optical* observations of the aurora to rely on; we do however note that ICEBEAR radar data is unequivocally and inexorably tied to the presence of aurorae (Ivarsen et al., 2024a, c, d, b, 2025a). In addition to this inference, we shall also demonstrate, during a data-rich conjunction study, that the source of our observed spectral density is, in fact, strongly linked with *auroral particle precipitation*, which by all intents and purposes *is* the aurora.

On 2 August 2023, an extended conjunction took place between ICEBEAR and the Japanese inner magnetosphere satellite Arase. During this conjunction, two additional ICEBEAR ~~–~~and CHAIN conjunctions took place. What follows is an analysis of the detected, *in-situ* electron flux observed by Arase during that conjunction, compared to the spectral density observations by our ground-based instruments.

Arase orbits Earth at a maximum distance (semi-major axis) of around 5 Earth radii, with a magnetospheric orbit that keeps the satellite relatively close to equator with an ionospheric footprint that routinely sample auroral latitudes (Miyoshi et al., 2018b, 2022): it has an apogee of 32,000 km and a perigee of 400 km, an inclination angle of 31°, and a period of 570 minutes. The satellite's magnetospheric location and ionospheric footprint during the conjunction are shown in Figure 6~~a–c)~~ a) to c), and we use the Tsy04 model for tracing the location of the satellite along Earth's field-lines (Tsyganenko and Sitnov, 2005). The satellite was located some 19° raised above magnetospheric equator, while observing a considerable flux of electrons with low pitch angles. Figure 6e) shows the particle observations, showing the total measured electron flux with low pitch-angles (close to 0°), for an extended period during which the satellite continuously orbited through regions mapping to regions of rather extreme E-region echo activity (Figure 6c). The satellite likewise observed some upper-band chorus waves (not shown), and we infer that the observed flux of low-pitch-angle particles is a proxy of the real precipitating particle flux, producing the characteristic diffuse aurora that we infer for this event.

The observed number flux relates to an energy flux (Redmon et al., 2017), which is readily converted to ionization rate altitude profiles (Fang et al., 2010), and we use the E-CHAIM model to convert this into a plasma density profile (Themens et al., 2017). In Figure 6f) we compare the estimated density profile (green line) with the measured altitude distribution of the observed radar echoes (red distribution).

During the 17-minute interval, ICEBEAR observed almost *4 million* individual echo locations, which we cluster using the Monte-Carlo model described in Section 2. Some 100 clustering spectra were calculated during this interval, and Figure 6d) plots the composite ICEBEAR ~~-~~and CHAIN spectrum for the entire interval.

Figure 7 plots, with black circles, 1-minute binned spectral index measurements, taking the initial ICEBEAR spectral index (the slope *before* the near-resolution fall-off), and comparing this to the initial CHAIN spectral index. This spectral interval goes over the injection wavelength or knee at ~ 5 km and provides a reasonably representative index of the larger wavenumber interval. In addition, in green hexagrams, we show the initial (overlapping) slope of the ISMR TEC spectra. A linear regression is applied to the spectral index results from the density curves. We note that the locations of both hexagrams are in excellent

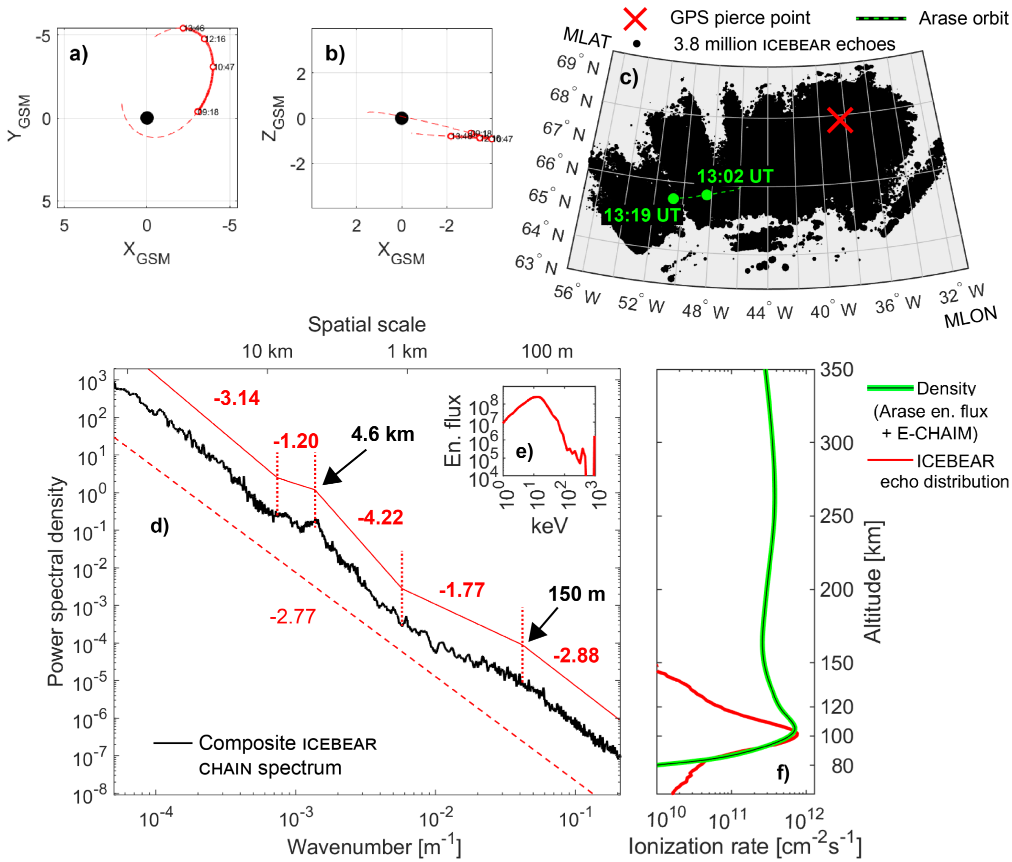

Figure 6. A space-ground-ground conjunction between ICEBEAR, CHAIN, and the Japanese inner magnetosphere spacecraft Arase that took place on 2 August 2023. **Panels a, b)** show the satellite location in the magnetosphere, in units of Earth radii, the black dot at the center being Earth itself. **Panel c)** shows the geospatial distribution of radar echoes in the E-region (black), with Arase's northern hemisphere ionospheric footprint plotted with green dashed lines [using the Tsy04 mapping method (Tsyganenko and Sitnov, 2005)], and the GPS pierce-point as a red cross, all in the field-line adjusted AACGM coordinate system (Baker and Wing, 1989). **Panel d)** shows the composite ICEBEAR -and CHAIN spectrum measured during the 17-minute interval starting at 13:02 UT on 2 August 2023. **Panel e)** shows the average precipitating electron spectrum measured by Arase during the interval, combining the low (LEP-e), medium (MEP-e), and high (HEP) energy particle detectors (Kazama et al., 2017; Kasahara et al., 2018; Mitani et al., 2018), and using pitch angles lower than 5° (LEP-e, MEP-e) and 10° (HEP). **Panel f)** shows, in red, the altitude distribution of ICEBEAR echoes and, in green, the plasma density altitude profile created by the precipitating particles measured by Arase using the E-CHAIM model (Themens et al., 2017) to incorporate the effects of solar extreme-ultraviolet photoionization.

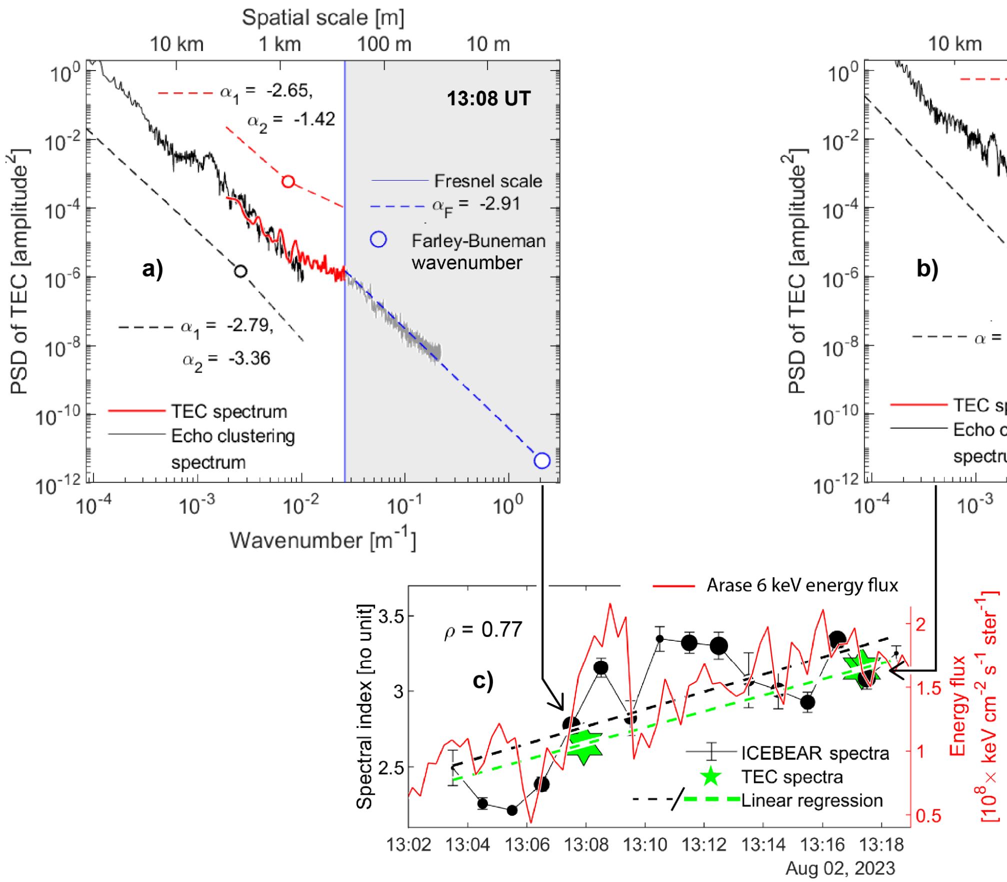

Figure 7. Panels a) and b) show two composite spectra, where the ICEBEAR clustering spectrum is shown in black and the TEC spectrum is shown in red and dark grey. A log-log two-component piecewise fit is shown for both spectra, as well as a linear fit for the TEC spectrum below the Fresnel-scale; spectral indices are indicated. Panel c) shows a timeseries of spectral index values, comparing α_1 from ICEBEAR (before the possibly noisy fall-off near 1 km), with α_1 from the CHAIN GNSS spectra. Some 100 ICEBEAR spectra observed during the interval 13:02 ~~UT–13~~to 13:19 UT are binned in one-minute bins, and are shown with black circles (with errorbars denoting the variability inside each bin) and α_1 from the two CHAIN TEC spectra are shown with green hexagrams. On the right axis we show the observed low-pitch angle ($\leq 5°$) flux of electrons measured in the 6 keV channel of the low-energy particle detector onboard Arase, selected for its high correlation with the spectral timeseries; 'ρ' indicates Pearson correlation at zero lag (see Figure 6 for details of the Arase conjunction).

agreement with the spectral index results. This being stated, we also note, that the event appears to have been a “two-plateau event" with a spectral index of -2.3 prior to 13:08 where the impinging fluxes were weaker and another value of -3.2 afterwards, following a marked increase in precipitation flux. The important point here is that there is a clear increase in slope magnitude (steepening spectra) in Figure ~~6g~~7c) that goes together with the unequivocal increase in the observed precipitating energy flux represented by the flux through the 6 keV channel of the MEP-e instrument (red line in Figure ~~6g~~7c).

So far, we have shown ~~the case for the spectral density comparisons (Figures 5c and 6g) where the observed spectra are *consistently steep*, for~~ that the observed composite spectra follow a single, continuous power-law decay at all wavenumbers except for prominent transitions near 5 km and near the Fresnel-scale around 270 m ~~. Based on Figure ?? as well, we ascertain, with some confidence, that these observed structures are *contained* within filamentary~~ (Figures 3e, 5c, d), and that the spectral index co-varies with the precipitating electron flux measured in the magnetosphere (Figure 7c). Prior conjunction studies have associated this same echo clustering with filamentary field-aligned ~~currents that are carried by the precipitating particles.~~ currents around diffuse aurorae (Ivarsen et al., 2023a, 2024a).

Added support for the foregoing ~~narrative~~ was also obtained from a separate statistical analysis gathered from two years of data. ~~That is to say, the overall steepness of the spectra that we have just discussed have been routinely found when filamentary FAC are present. To be specific, the~~ The inferences made from the 10 ICEBEAR and CHAIN conjunctions are backed in Figure 8a) by the index distribution of 7,700 ICEBEAR clustering spectra observed during the two years 2020, 2021 [the same database that was used in Ivarsen et al. (2023b)]~~. In Figure 8a), this distribution is~~ , shown with a dark red line~~, and its shape and mode (peak)agree with the foregoing, namely, we observe a consistently steep spectral shape with the most probable spectral index being close to -8/3.~~ . The ten composite spectra carry fitted overall indices between -1.93 and -2.83 (Figure 8d), with mean -2.50, median -2.52, and standard deviation 0.24 (mean -2.56, standard deviation 0.15 when the single shallowest event is excluded), while the radar-only distribution peaks at -2.7. The conjunction sample thus lies within the radar-only climatology, which is conditioned only on echo activity: the scintillation selection described in Section 2.3 does not produce anomalous spectral shapes, and the scale-free organization is not an artifact of that selection.

Thus, Figure 8 ~~clearly~~ demonstrates a consistent tendency ~~for a value around $-8/3$ as the most probable measurement value overall, and~~ in the spectral indices, with a relatively narrow spread ~~around that value~~about the most probable values between -2.5 and -2.7 [in the two-dimensional convention of Section 2.4]. The echo altitude distribution ~~is also shown~~ for the 10 events, shown in Figure 8~~d)~~c), peaks at 102 km. Using this altitude for the GPS pierce points gives us a phase screen drift of around 500 m/s, coinciding with the peak of the median Doppler speed distribution for the 10 events (Figure 8b). ~~As discussed above the only reasonable explanation for~~ The explanation most consistent with this signature is that those structures are Farley-Buneman waves that reach their largest amplitudes at the ion acoustic speed, just as is observed in HF and VHF radars; we weigh this interpretation against alternatives in Section 4.1. This ~~important observation confirms~~ observation indicates that the GPS scintillations ~~not only~~ took place in the E-region, a notion supported by recent statistical studies (Blinstrubas et al., 2025), ~~but~~ and that they were ~~also~~ caused by long-wavelength (270 m) Farley-Buneman-liketurbulence.

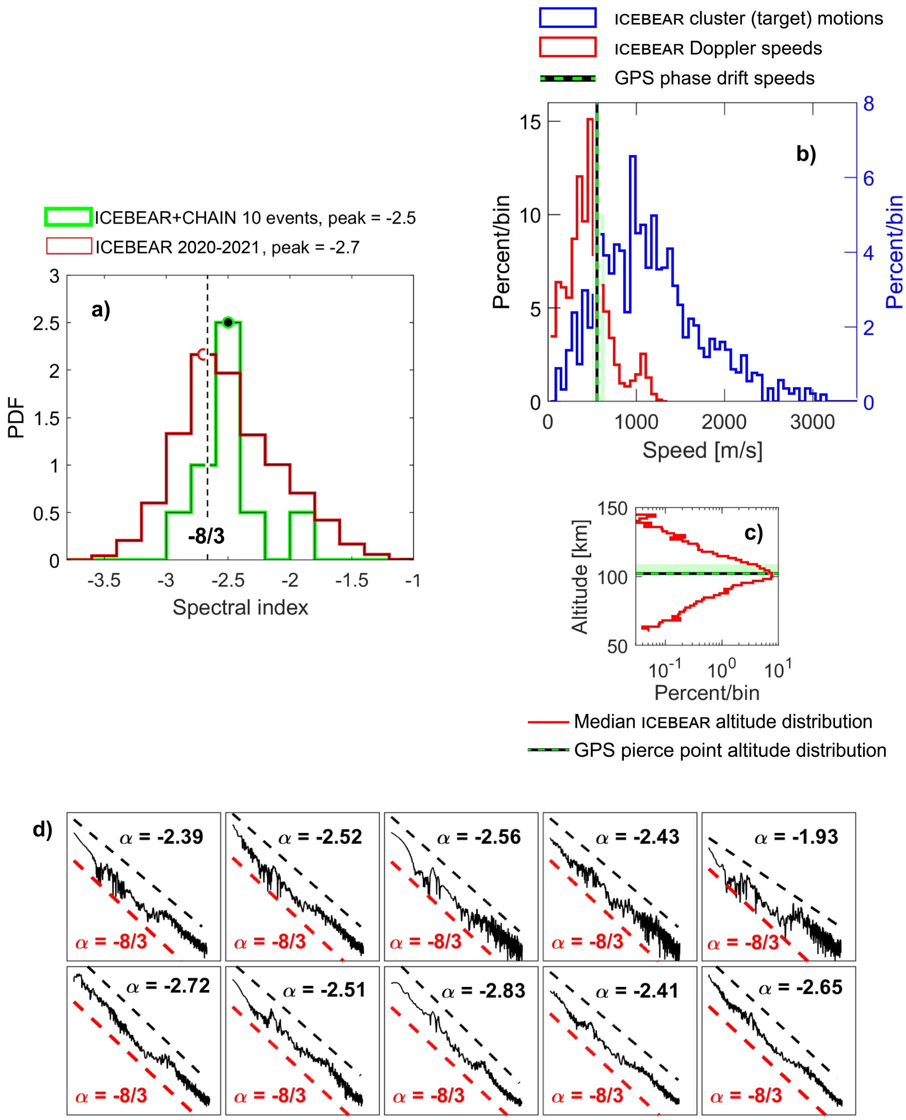

Figure 8. Panel a) compares the ICEBEAR ~~-~~and CHAIN spectra (green line) with a statistical aggregate of 7,700 ICEBEAR echo clustering spectra (red line) observed during 2020, 2021 [the database that was analyzed in Ivarsen et al. (2023b)]. **Panel b)** shows the mean distributions in VHF radar Doppler speeds (red histogram), the mean distribution in observed echo cluster (target) motion (blue histogram), and the average GPS phase drift speed (green and black line). **Panel c)** shows the distribution of echo altitudes, with a black-and-green line indicating the assumed GPS pierce-point locations (with shaded green region giving upper/lower quartile distributions). **Panel d)** shows all 10 composite ICEBEAR ~~-~~and CHAIN spectra (solid black line), with a linear log-log fit (black dashed line) and a ~~-8/3-slope~~ reference slope of $-8/3$ (red dashed line; $-5/3$ in the one-dimensional convention) indicated.

4 Discussion

There are two prominent and, to a certain extent, unexpected results in the present study. First, the observed radar Doppler speeds agree remarkably well with the GPS phase drifts, while being clearly much smaller than the tracked echo motions. The second prominent result is the ~~seemingly universally steep~~ near scale-free power spectra that we observe with ICEBEAR and CHAIN. We shall now discuss these points in order.

4.1 Long-wavelength Farley-Buneman waves and their fate

As has been repeatedly pointed out in references cited above, the Doppler speeds extracted from VHF radars in the auroral electrojet typically do not exceed the E-region ion acoustic speed, with due exceptions associated with narrow spectra extracted from the edge of the instability cone in the upper part of the unstable E-region (St-Maurice et al., 2023). This being stated, the E-region cluster motions extracted from ICEBEAR as a target radar are clearly much faster than the ion-acoustic speed when the electric field is very strong. The target motions correspond to the motion of magnetic field tubes drifting at the $\mathbf{E} \times \mathbf{B}$-drift while said field tubes are exciting large-amplitude ion-acoustic waves for a brief moment during which the electric field locally must go down to the Farley-Buneman threshold value (Foster and Erickson, 2000; Oppenheim and Dimant, 2013; St.-Maurice and Hamza, 2001). Thus, the sources of the ion-acoustic waves are moving at a drift that matches the F-region plasma drifts. This feature has been exemplified in Figure 5a, b), and in recent literature on the subject (Ivarsen et al., 2024c, d).

We have to consider the fact that the Fresnel-scale (~ 270 m) structures also exhibit GPS phase drifts moving at the ion acoustic speed rather than at the $\mathbf{E} \times \mathbf{B}$-drift. Gradient-drift waves are not constrained by the ion-acoustic speed. Even if, like the smaller m-size structures, they were to grow to an amplitude such as to reach threshold conditions, the balance would involve chemistry and diffusion, not ion inertia and diffusion. However, since the 270 m waves move at the ion-acoustic speed when their amplitude is the largest (which is what we observe), the simplest explanation for this result is that the observed Fresnel-scale structures are ~~, in fact,~~ controlled by ion-inertia, i.e. they are *Farley-Buneman (FB) waves*. However, according to the standard linear fluid theory for altitudes between 100 and 105 km, the growth rates expected are 10,000 times smaller at 270 m than at 2.7 m. That is to say, the growth rates are given by ~~$Ck^2(Vd^2 - C_s^2)$~~ $Ck^2(V_d^2 - C_s^2)$ where C is a well-known constant, V_d is the relative drift between ions and electrons (basically E/B at those altitudes) and C_s is the ion-acoustic speed (Fejer and Kelley, 1980). The k^2 dependence can be compensated to a certain extent if the electric field is itself ~ 10 times stronger than the threshold value (200 mV/m as opposed to 20 mV/m). In that case, the growth rate picks up by a factor of 100 and the factor 10,000 is down to a factor 100 compared to the growth rate of meter-size FB waves probed by radars under ordinary electric field conditions. Put in another way, in spite of weaker growth rates, it might be feasible to excite FB waves at a couple of hundred meters, particularly when the electric fields are *strong*. This being stated, ~~?~~ Oppenheim et al. (2008) have seen evidence in their numerical simulations for nonlinear 160 m structures growing at a much faster rate than expected from linear theory. They attributed the growth to an energy extraction from the smaller scale FB waves, i.e., to what could be described as a reversed, or inverse, cascading process.

Still, the fact, that the *FB waves* are observed to move at the ion-acoustic speed, requires a comment in view of seeing *270 m-sized waves* move at that speed. First of all, a high-resolution Continuous Wave (CW) experiment has shown that FB waves are at first moving much faster than at the ion-acoustic speed, but that as their amplitude grows they reach a much larger amplitude at the ion-acoustic speed after which they simply disappear quickly (Prikryl et al., 1988, 1990). This means that the meter-size FB waves follow linear theory expectations at first but that as they grow in amplitude, they reach a maximum amplitude at the ion-acoustic speed, after which they quickly disappear. Radars are biased to the largest amplitude structures and therefore see them moving at the ion-acoustic speed (or slower depending on the line-of-sight). We note that one may wish to use the word “threshold speed" instead of “ion-acoustic speed." In particular, electron heating perturbation effects modify the threshold speed below 100 km altitude and ion heating perturbations would also matter above 110 km [see St.-Maurice and Chau (2016) for a comprehensive review of the situation]. Given that the observations presented here are mostly from the 100 to 105 km altitude region, the threshold speed and the ion-acoustic speed are very close to being one and the same.

Numerical simulations have indeed found that the largest amplitude waves move at the ion-acoustic speed in a direction roughly matching the ExB direction (Dimant and Sudan, 1995). Theoretical work has involved anomalous diffusion (Robinson, 1986), mode-coupling explanations, for example in Hamza and St-Maurice (1993) & references therein, and double polarization effects, as per the work by Sato (1972) and St.-Maurice and Hamza (2001). These notions all use the fact, in one way or the other, that the unstable situation introduces a polarization electric field that moves electrons *against* the original electric field direction, thereby damping the electron fluid. This is a wave-particle interaction that affects the nature of the local energy expenditure. For instance, Sato (1972) and St.-Maurice and Hamza (2001) used a relatively simple approach by considering structures that, while initially elongated, were not ideal plane waves. The two-dimensionality leads to a decrease in the electric field inside the waves as the wave grows. We note the circularity in this situation, as the electric field evidently works to move charges, but at the same time also extinguishes itself, which weakens local charge motion. The rapid feedback stops when the electric field is at threshold conditions. This is what saturates a Farley-Buneman wavefield, and the work done in causing this saturation is substantial.

On that note, the FB waves also have a nonlocal character, as their eigenfrequency is a small but non-negligible function of altitude, i.e. of position along the geomagnetic field (Drexler et al., 2002). This introduces vertical shears that short-out the electrostatic fields and dissipate the waves while heating the electrons (Maynard et al., 1973; Vickrey and Kelley, 1982; St-Maurice and Goodwin, 2021; Zhang and Varney, 2024; Ivarsen, 2026). In this light, even if the growth rate of 270 m waves is from an inverse cascading process, a final nonlinear evolution has to limit the growth through the kind of mode-coupling or double polarization effects described above, since the principle applies to initial elongated structures of any width or size. As a result, 270 m structures at 102 km end up at the ion-acoustic speed as long as they are the byproduct of the FB instability, be it through linear or nonlinear growth processes.

Alternative interpretations deserve consideration. Gradient-drift structuring at these scales is expected around aurorae, mixed regimes in which GD structures host embedded FB activity are well documented, and nonlinear coupling between the two can transfer energy across the Fresnel scale without a pure FB origin (Sudan et al., 1973). What the velocity comparison constrains is the motion of the scattering structures at their largest amplitude: gradient-drift structures advect with the $\mathbf{E} \times \mathbf{B}$ drift and are not bound by the ion-acoustic speed, whereas the observed phase screen drifts are consistent with the ion-acoustic speed and well below the concurrent target motions (Figures 4b and 8b). The observations are therefore consistent with long-wavelength FB-like structures dominating the scintillation-producing scales in these strong-field events, while a mixed GD and FB scenario cannot be excluded, in particular one in which GD fingers provide the seed gradients for FB growth. We also recall that the event sample is conditioned on amplitude scintillation (Section 2.3), so the statement is about scintillation-producing events under strong driving, and does not extend to the quiet electrojet. The velocity discrimination itself rests on the phase screen assumptions bounded in Appendix B; within those bounds, the separation between the phase screen drift (~ 500 m/s) and the target motion (~ 1000 m/s) is an order of magnitude larger than the combined measurement uncertainty.

4.2 ~~Universally steep power spectra in filamentary FAC regions~~

4.2 Scale-free spectral organization in the auroral E-region

~~Every time we had FAC data from satellites, the steep spectral slopes with indices of about -8/3 were observed in diffuse auroral regions and intense filamentary FAC structures . This is not surprising, since current filaments are associated with Alfvén waves, and the mode of the spectral slopes (not its spread)confirm this fact. We need to stress that not all the events were associated with slopes and with FAC filaments, which is consistent with a minority of cases for which the spectral slope was clearly not so steep (as seen with minor but real deviations from the overall statistics in Figures~~ The central property of the composite spectra is not the value of the index but its constancy. Away from the two knee regions, the piecewise segment indices are consistent, within the fitting spread, with the overall single-fit values summarized in Figure 8, and the same index distribution recurs in the scintillation-independent radar-only climatology of 7,700 spectra. A minority of spectra deviate from the overall statistics, as seen in Figures 8a and 7c~~above). The fact remains that a vast majority of cases were associated with filamentary FAC and Alfvén waves. This underscores an important fact: while not quite all spectra had a -8/3 spectral index, when they did, the spectral slope~~ , and where the power law held, it extended to all scales available to our scrutiny, down to 20 m.

~~We already know that Alfvén waves were involved in the observed filamentary parallel current regions (Figure **??**~~The value of the index, by itself, selects no mechanism: it is tied to the measurement convention (Section 2.4), and ~~the associated power spectrum has a -8/3 spectral power index. This wave spectrum has been associated with kinetic magnetohydrodynamic (MHD) turbulence , in particular kinetic Alfvén waves (KAWs), (Boldyrev and Perez, 2012; Chen et al., 2013; Galtier and Meyrand, 2015; David a . Those waves are generated in the warm magnetospheric plasma. They propagate into the cold collisional ionosphere, where they transition into inertial or dispersive Alfvén waves, in the process, preserving the spatial scaling of~~ several turbulence and instability frameworks predict values within the measurement spread in either convention. We therefore attach no interpretation to the value, and we have avoided cross-convention comparisons with published one-dimensional indices throughout. What the composite measurement establishes is the continuity of a single spectral organization across four orders of magnitude in scale, through both knees, from tens of kilometers down into the domain where FB waves demonstrably control the dynamics. Together with the velocity agreement in Figure 8b), this continuity is consistent with the two instruments sampling one contiguous turbulent field whose small-scale end is governed by the FB instability, as the ~~driver. The waves are reflected back or are absorbed by the plasma. This modulates the local electric field. As we have reported here, in~~ velocity comparison demonstrates at the ~~E-region, these structured electric fields instantly trigger turbulent dissipation, notably through the Gradient-Drift Instability (GDI) and the FB. The question to ask is : how is it that in spite of the clear presence of abundant FB waves (as observed by ICEBEAR) the spectrum keeps a distinct -8/3 Alfvén wave signature for all scales available to our scrutiny, that is, down to at least 20 m, long past the 270 m mark where FB waves are evidently causing the structure?~~ Fresnel scale.

Consistent with the notion of a trigger of ionospheric plasma instabilities, we note that the ~~steep~~ spectra are interrupted by two knee regions, one near 5 km wavelength and the other near 200 m. Injection wavelengths of the order of 5 km are typical of scales associated with the largest Gradient-Drift (GD) waves found in the equatorial electrojet region. At the equator, they are triggered by electric fields of the order of 15 mV/m or greater in combination with vertical density gradient scales of the order of 10 km (Tsunoda et al., 1982). Somewhat larger size GD waves are possible, but at some point their growth is limited by chemical recombination when the latter becomes faster than the gradient contribution to the growth rate. We note that, in the equatorial regions, GD waves can modulate small scale FB waves if the ambient electric field exceeds 15 mV/m. Also, GD waves have been proposed as a seed for FB waves: as unstable fingers associated with GD structures move into increasing low density regions, the gradients on their side could steepen to the point that the instability threshold of FB waves is achieved (Sudan et al., 1973). Although there are clear physical reasons to *expect* a break-point at kilometer scales in our observations (see, e.g., Ivarsen et al., 2021, for a systematic tendency for kilometer-scale breakpoints in F-region auroral plasma turbulence observatio , we note that these scales are relatively close to the spatial resolution of ICEBEAR's imaging algorithm, and so we urge a degree of caution in their interpretation.

The other knee at ~~200-300 m seems to be~~ 200 to 300 m is directly associated with the Fresnel size of structures seen near 102 km ~~. We~~ (as the GNSS spectra are conditioned on the presence of GPS amplitude scintillations). That said, we found, unexpectedly, that ~~those waves are~~ the velocity signature of those structures is consistent with FB waves in spite of their large size, i.e., of their weak linear growth rates. ~~However, since the growth rate~~ Since the growth may be linked to nonlinear "inverse cascading", it is tempting to assume that this match between the knee and the Fresnel-scaleFB structure is not a coincidence and that this describes the largest FB waves in the system. However, the GPS events analyzed in this paper were selected for exhibiting strong amplitude scintillations, and so there is likely a selection effect favouring Fresnel-scale energy injection events~~.~~; the knee position, unlike the spectral indices surrounding it, should therefore be generalized with caution.

A third component of the puzzle is the density of FB irregularity bursts monitored by ICEBEAR. As stated in a preceding section, FB waves are ephemeral and can come and go in a fraction of 1 s. Both theoretical and numerical works indicate that the maximum amplitude of these waves is not increasing dramatically with electric field strength. Instead, what increases is the abundance of the FB waves. This is not intuitively difficult to understand since stronger electric fields mean faster linear growth rates, meaning more growth events per unit time, meaning more growth episodes per unit space. The growth in the number of large amplitude scatterers has in fact been demonstrated in spectacular fashion in the work of Ivarsen et al. (2025a) who found the density of large amplitude ICEBEAR radar echoes to simply be proportional to the electric field when such field exceeded 40 mV/m ($E/B >$ 800 m/s), A final aspect to keep in mind is that FB waves are very efficient at extracting energy from Hall currents and giving it back to particles. This is not Joule heating *per se*, as it involves extracting kinetic and potential electric energy from the currents which then turns into a quick dissipation involving the creation by nonlocal processes of wave parallel electric fields and currents carried by electrons, which then give the energy gained from the resulting acceleration to the background gas through elastic and, mostly, inelastic collisions (see Section 4.1).

We arrive at the conclusion that powerful Alfvén waves transfer an unusual amount of their energy to FB waves by creating larger FB structures (which always have more energy than smaller structures) and by creating a number of such structures that increases proportionally to the electric field imposed by Alfvén waves, and, more generally, ULF waves see Shen et al. (2024); Ivarsen et al. (2025a), as well as the present study's own companion paper. As a result of this increase in dissipation rate through unstable transient ionospheric structures, the Alfvén wave spectrum is able to keep its -8/3 spectral index. In other words, the ionospheric structures are in lock-step with the Alfvén wave spectrum.

While there is clearly a need for future quantification, it remains an observational fact that the large-scale organization that emerges from packing thousands or millions of FB waves inside a limited volume is universally steep close to scale-free across four orders of magnitude in scale-size. We suggest here that incoming Alfvén waves are modulating the local electric field, on all scale-sizes, akin to the argument constructed by Ivarsen et al. (2024a). The "pre-structured" injections drive instabilities, and the fastest evolving instabilities (FB waves) are used to maximize the energy extraction from Alfvén waves. The The bursty nature of the FB structures actually helps maximize the rate of energy extraction and transfer it from the driving currents and its transfer to the ambient gas.

The notion that Alfvén waves are directly structuring the A quantitative account of how magnetospheric drivers imprint the observed spectral organization remains open. Recent statistical work has correlated E-region yields immediate explanatory power for the magnetosphere-ionosphere coupling. The coupled system would evolve toward a state of maximum energy dissipation, governed by Alfvénic impedance matching and wave reflection: Particle precipitation that fails to reach the altitude with the lowest instability threshold (St-Maurice et al., 2023) may cause impedance mismatch for the incoming Alfvén waves, causing Alfvénic power to be reflected rather than dissipated. Consequently, the coupled system selectively sustains, and favours, precipitating electrons whose emission profile peak at altitudes around 105 km where the FB instability threshold is lowest, offering a thermodynamic explanation for the preferred altitude of pulsating auroras (Hosokawa and Ogawa, 2015; Partamies et al., . What is more, non-linear wave heating in the upper part of the unstable layer suppresses dissociative recombination rates ($\propto T_e^{-1/2}$, Schlegel, 1988). It may even be that the subsequent net increase in conductance may provide a significant contribution to the problem of the "saturating polar cap potential" (see, e.g., Siscoe et al., 2004). In this regard, Section **??** presents observations from Swarm that indicate the satellite in fact observed Alfvén waves that were absorbed without reflection, which is, incidentally, the most efficient way to dissipate electromagnetic energy in our atmosphere.

We further speculate that the consistently steep $-8/3$ can be described in terms of a self-organized criticality, in which the dissipation performed via Alfvén waves is locked or saturated against FB waves. This eventuality needs further scrutiny, and , in a companion paper, we follow the notion to a logical conclusion, through the lens of the renormalization group, a device intimately suitable for the topic of space weather model "sub-grid" parameterizationstructuring with ULF wave activity and magnetospheric particle dynamics (Shen et al., 2024; Ivarsen et al., 2025a), and the Arase conjunction presented here ties spectral steepening directly to the precipitating electron flux, a comparison of the same observable with itself and hence independent of spectral convention. Establishing a causal chain from a specific magnetospheric wave population to the E-region spectrum requires convention-consistent spectral comparisons across altitude, and we defer that question to future work.

5 Conclusion

Using a novel measurement technique, we have resolved the power spectral density of the E-region ionosphere across four orders of magnitude in spatial scale. ~~We found that in filamentary upward field-aligned current regions, the auroral plasma preserves the structure of its magnetospheric driver, exhibiting the characteristic $k^{-8/3}$ scaling of kinetic Alfvén turbulence~~The composite radar and GNSS spectrum measures the two-dimensional spectral density of the turbulent irregularity field, and across ten conjunction events it exhibits a near scale-free decay, with overall spectral indices of -2.50 ± 0.24 in that convention, interrupted by reproducible break points near 5 km and near the Fresnel scale at 270 m. We also found that the 270 m structures associated with Fresnel scales in GPS scintillations were drifting at the ion-acoustic speed~~. This was made very clear; for our samples,~~: the GPS-inferred drift ~~not only~~ matched the expected value for the ion-acoustic speed ~~, but it was also much smaller than~~ while remaining well below the plasma $\mathbf{E} \times \mathbf{B}$ drift inferred from the ICEBEAR target motions in the same region (see Figures 4b and 8b). This ~~means that~~ velocity signature is consistent with the 270 m structures~~(~~, which matched the position of a knee structure in the overall spectrum~~) were actually~~ , being long-wavelength Farley-Buneman waves, ~~just~~ like the much smaller scale 3-m waves detected by the ICEBEAR radar. Since the linear FB growth rate at 270 m should be very small, this observation came as a surprise. The observation ~~seems~~agrees, however, ~~to confirm~~ with results from numerical simulations that found that large scale FB waves were excited nonlinearly through an *inverse cascade* ~~(?)~~(Oppenheim et al., 2008). The presence of such large-scale FB waves means that there can be far more energy dissipated by FB waves than if only ~~less than 10-m structures~~ structures smaller than 10 m had been destabilized.

In closing, we note that the ionosphere's bottomside, the E-region, has been ascribed many roles. In-situ satellite observations not being possible we were left with short-lived rocket campaigns and a handful of incoherent scatter radars and only somewhat more numerous coherent radars (Palmroth et al., 2021). Still the technology has become sophisticated enough to add, over time, several new perspectives and insights. In the process the E-region has become more than just a region to pass Pedersen currents that offer a closing of the magnetosphere-ionosphere current system, with attendant Joule heating and ~~preciptiating~~ precipitating particle energy dissipation rates. While these features are very important, the addition of fast temporal and much finer spatial resolution than before by ground-based instruments is producing a much more complex picture. We have highlighted a few of the new capabilities in the present paper, to which could be added many important results from incoherent scatter radar showing how dynamical the E-region can be (e.g., St-Maurice et al., 1990; Blinstrubas et al., 2025). The present study has continued the march towards new important insights by advancing our understanding of auroral plasma turbulence, with the new extraction of the composite ~~radar–GNSS~~ radar and GNSS power spectrum.

Appendix: ~~Geospace conjunction studies~~

~~This Appendix supports the findings presented in the main text, by providing technical, theoretical, and observational details concerning the many multi-instrumental conjunctions that we analyze.~~

~~The Appendix is organized as follows. Section A (Figure A1) describes the core dataset used in the Main Paper, namely the ten ground-ground conjunctions between the experimental VHF radar ICEBEAR and the Rabbit Lake GPS receiver in the CHAIN network of ionospheric scintillation monitoring receivers (ISMRs). Section **??** (Figure **??**) describes an extended space-ground-ground conjunction between ICEBEAR, CHAIN, and two European Swarm satellites.~~

Appendix A: Ten ~~ICEBEAR-CHAIN~~ ICEBEAR and CHAIN conjunctions

Figure A1 showcases six simultaneous ICEBEAR ~~-~~and CHAIN conjunctions, occurring in rapid succession during two extended events that took place on 7 July 2023 and 18 August 2022. Each panel of Figure A1 shows the composite power spectrum for each conjunction event. We normalize the power amplitude to facilitate a direct spectral shape comparison, and we apply an automatic spectral slope- & break-point detection algorithm based on piecewise linear Hermite polynomials (D'Errico, 2009), with close details described in, e.g. Ivarsen et al. (2019), and Ivarsen et al. (2021). For scale-sizes between 750 m and 3000 m the spectral shapes from the two different methods are observed to match strikingly well. What is more, the steep slopes at the larger scales (>1 km) are highly consistent with the steep slopes seen at smaller scales (<100 m), with observed spectral index values between -2.6 and -3.1. A prominent break-point is observed near the Fresnel-scale, and similar prominent features are visible at scale-sizes around ~~1–10~~1 to 10 km, both in accordance with expectations based on plasma instabilities from the literature (Villain et al., 1986; Ivarsen et al., 2023b; Basu et al., 1990; Mounir et al., 1991; Spicher et al., 2014; Hamza et al., 2023).

Appendix B: ~~Extended ICEBEAR-CHAIN-Swarm conjunction~~Sensitivity of the Fresnel scale and scan velocity to the phase screen assumptions

~~We shall describe two successive space-ground-ground conjunctions that offer a clear, physical interpretation of the composite spectra. Figure **??** details two triple conjunctions between ICEBEAR, CHAIN, and the European Space Agency's Swarm mission (Friis-Christensen et al., 2006; Wood et al., 2022), consisting of three polar orbiting satellites (inclination 87°, altitude ~ 450 km, and orbital period of 90 minutes).~~

~~The conjunctions, with their geospatial coordinates detailed in Figure **??**c), exhibited very strong magnetic fluctuations perpendicular to Earth's magnetic field, produced by field-aligned currents, and what follows is a treatment of the structure, or *filamentation*, of those currents.~~

~~Two space-ground-ground conjunctions, and one ground-ground-conjunction, between ICEBEAR, a CHAIN ISMR, and the Swarm A and C satellites, on 6 May 2023. Panel b) shows the spatial distribution of echoes (black point-cloud), with the Swarm satellite orbits (blue lines) and GPS pierce-point (red circle) superposed. Panels a) and f) show the magnitude of the~~

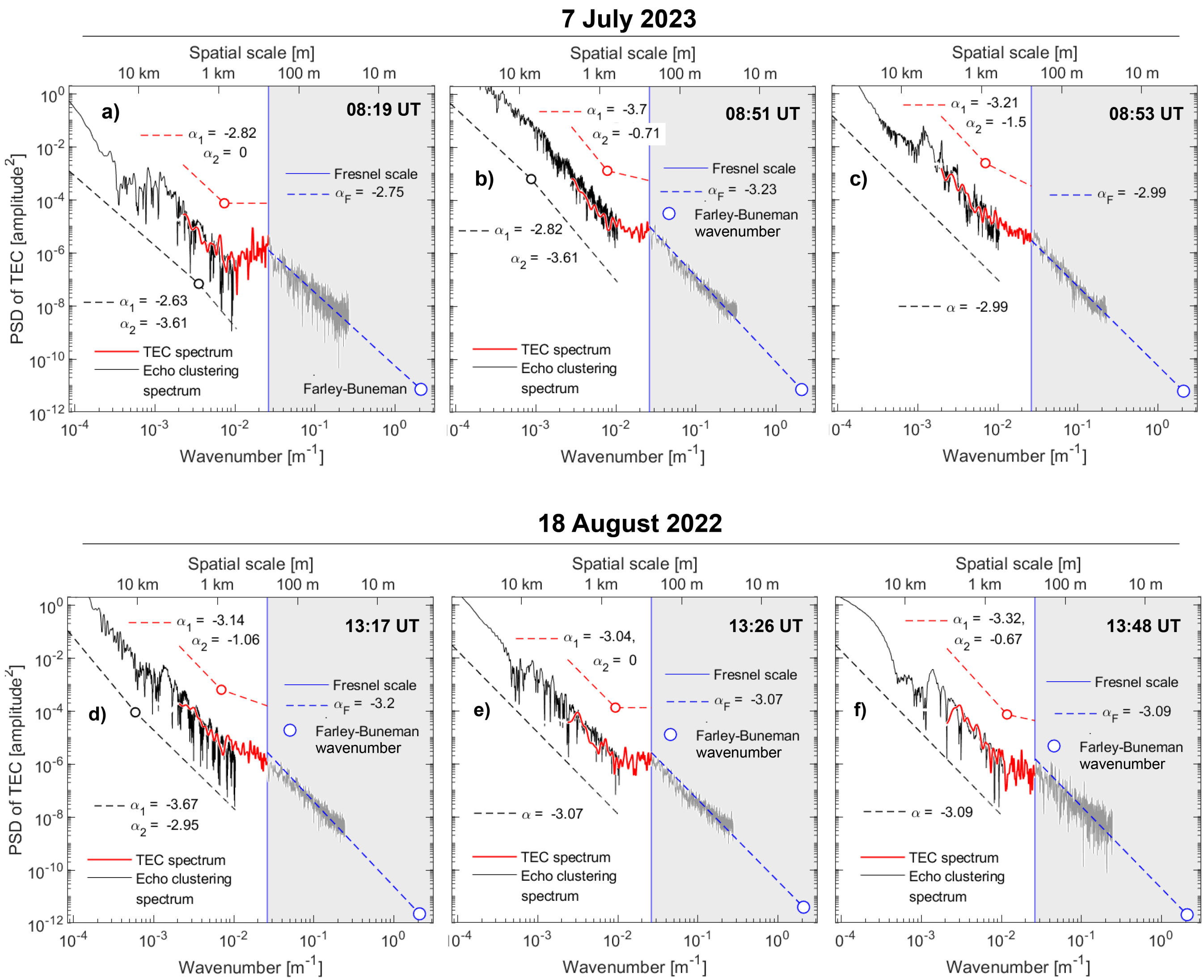

Figure A1. Six simultaneous ground-ground conjunctions between the ICEBEAR radar and observations from the CHAIN ISMR in Rabbit Lake. Each panel compares the spectral density measurements, the internal structure of the radar point-clouds denoted by a black line and the spectrum of GPS amplitude fluctuations in red and gray colors. The spectral indices are calculated automatically following Ivarsen et al. (2019) and are indicated, as is the Fresnel-scale.

~~perpendicular magnetic fluctuations observed by the Swarm satellites (black line and blue colorscale), with the latitudinal distribution of ICEBEAR echoes superposed in red. Panels b,d,e, and g) show various composite powerspectra, with ICEBEAR clustering spectra (black), compared to CHAIN k-spectra (red, gray) and field-aligned current structuring spectra (blue) measured by Swarm. Panel e) shows an enlarged portion of the composite ICEBEAR-CHAIN spectrum in panel d).~~

~~Following Ivarsen et al. (2023a) and Ivarsen et al. (2024a), we Fourier analyze the Swarm 50 Hz magnetic field fluctuations transformed into a mean-field-aligned coordinate system (Park et al., 2017; Ivarsen et al., 2020), and this Fourier analysis yields information on electrical current filamentation, the degree to which the observed currents are non-laminar, or anomalous. The quantity is analogous to the structuring of magnetic field-tubes in the plane perpendicular to the geomagnetic field. Figure ??a, f) detail the observed magnitude of the perpendicular magnetic fluctuations, with the distribution of simultaneously observed ICEBEAR echoes superposed with a red line.~~

~~As the Swarm satellites orbit through the topside (F-region) ionosphere with a velocity of $v_s = 7.62$ km/s, we apply Taylor's "frozen-in"-hypothesis to convert the temporal powerspectra to k-spectra. These are superposed on the ICEBEAR echo clustering spectra in Figure ??b, g), showing reasonable agreement on a wide range of spatial scales, that is, between 10^5 m and 750 m. We again note a good shape-wise agreement between the radar clustering spectra and the observed field-aligned current structures (filaments), echoing recent studies (Ivarsen et al., 2023a, 2024a). The implications are that the spatial characteristics of turbulence in the E-region are contained, communicated, or embedded, by filaments in the field-aligned currents.~~

~~In Figure ??d, e), we compare the ICEBEAR and GPS spectra, for which the simultaneous conjunction took place between the two satellites' orbit, and which again exhibit excellent shape-wise agreement down to individual spectral features around 1 kilometer (inset panel e).~~

Appendix C: ~~Sensitivity of the Fresnel scale and scan velocity to the assumed irregularity altitude~~

In Section 2.3, we derived the corrected Fresnel scale λ_F (Eq. 3) and the phase-screen scan velocity $v_d = f_F \lambda_F$, where f_F is the Fresnel frequency derived from the data, and we did so under the assumption of a single, thin irregularity layer at altitude $h = 105$ km. Because the ICEBEAR echo altitude distribution (Figure 8c) spans roughly ~~95–110~~95 to 110 km with an overall peak near 105 km (Ivarsen et al., 2023c), it is important to quantify how sensitive these derived quantities are to the ~~thin layerassumption.~~ assumed altitude. We then bound the three remaining assumptions that enter the velocity comparison: the motion of the pierce point itself, the finite thickness of the scattering layer, and the assumed isotropy of the irregularities. Table B1 lists the ten conjunction events with the GPS space vehicle (PRN) and elevation angles that enter these bounds.

From Eq. (3), $\lambda_F \propto \sqrt{h}$, with the satellite elevation angle θ entering as a multiplicative factor in the denominator. The fractional error in λ_F due to an altitude offset Δh from the assumed value $h_0 = 105$ km is therefore

$$\frac{\delta \lambda_F}{\lambda_F} = \sqrt{1 + \frac{\Delta h}{h_0}} - 1, \tag{B1}$$

which is independent of θ, and v_d subsequently inherits the same fractional sensitivity. Figure B1 confirms this: panel a) shows λ_F evaluated across the ~~90–120~~90 to 120 km altitude range for representative elevation angles, while panel b) shows that

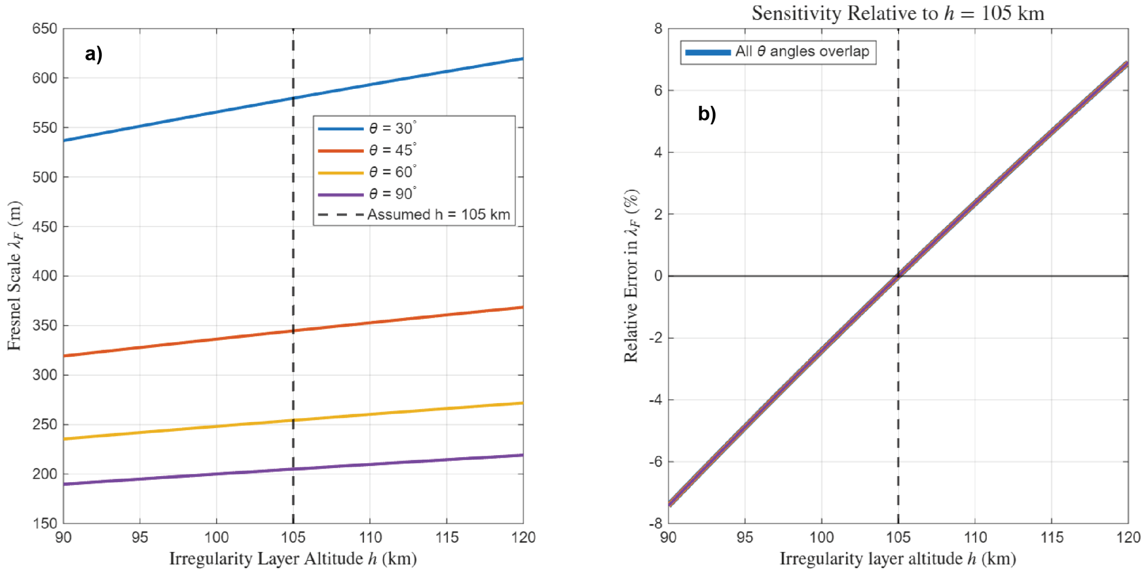

Figure B1. **Panel a):** λ_F as a function of altitude, for representative elevation angles. **Panel b):** the relative error curves (Eq. B1) for all θ.

the relative error curves for all θ collapse onto a single curve. A physically significant ± 5 km deviation from the assumed altitude introduces a relative error of less than 2.5%, corresponding to a scan-velocity uncertainty of approximately ± 10 m/s for a typical observed drift of 500 m/s. This uncertainty is small compared to ~~tupical~~ typical values of the E-region ion-acoustic speed (~~~400–500~~400 to 500 m/s). In wavenumber space, a 2.5% shift in λ_F displaces the Fresnel break-point by ~0.01 decades in k.

~~**Panel a):** λ_F as a function of altitude, for representative elevation angles. **Panel b):** the relative error curves (Eq. B1) for all θ.~~ The scan velocity measures the relative motion between the ionospheric pierce point (IPP) and the drifting irregularities, so the motion of the IPP itself enters the comparison with the radar velocities. For a stationary receiver, the IPP velocity at the shell height scales as the satellite velocity transverse to the line of sight, multiplied by the ratio of the receiver-to-IPP and receiver-to-satellite distances. The receiver-to-IPP distance is $h/\sin\theta$, below 120 km for the elevation angles in our sample (Table B1, all $\theta \geq 60°$), while the receiver-to-satellite distance exceeds 2×10^4 km for GPS orbits; with GPS transverse velocities below 3.9 km/s, the IPP speed at a 102 km shell is bounded below roughly 25 m/s. This is under 5% of the observed 500 m/s drifts, comparable to the altitude uncertainty derived above, and an order of magnitude below the separation between the phase screen drifts and the target motions. The same bound covers the projection geometry: since the IPP motion contributes at most a few percent of the relative velocity, the scan direction is set by the irregularity drift itself, and the azimuth of the satellite track does not materially affect the inferred speed.

The thin-layer approximation assigns all phase perturbation to a single altitude. A finite layer of thickness Δh centred on h_0 instead distributes the Fresnel scale across the layer, with the spread given by Eq. (B1) evaluated at the layer edges: for a full thickness of 15 km, matching the echo altitude distribution in Figure 8c), the spread in λ_F is below $\pm 4\%$. A finite layer therefore broadens the Fresnel knee and its associated spectral oscillations without displacing the knee centre or altering the asymptotic slopes, consistent with the weak-scatter treatment in Ivarsen et al. (2026). The weak-scatter approximation itself requires moderate scintillation (S_4 below roughly 0.5); in saturated scatter, multiple scattering would flatten the amplitude spectrum and the slope relations of Section 2.4 would fail.

Finally, Section 2.3 treats the base irregularities as isotropic in the plane transverse to the ray. Strong field-aligned anisotropy would modify the amplitude of the phase spectrum through a geometry factor and, under oblique propagation, could bias the inferred drift when the scan direction aligns with the structure elongation. Two observations bound this effect empirically: the elevation angles in our sample are high (Table B1), limiting obliquity, and the phase screen drifts agree with the radar Doppler speeds (Figures 4b and 8b), a measurement that is unaffected by the phase screen geometry. For that agreement to be an artifact of the geometry, the anisotropy would have to bias drifts near 1000 m/s down by a factor of two, far in excess of any elevation-dependent correction at these angles, and land them on the peak of the independently measured Doppler distribution.

Table B1. The ten ICEBEAR and CHAIN conjunction events. All GPS signals were recorded by the CHAIN ISMR at Rabbit Lake; PRN denotes the GPS space vehicle, and θ the median elevation angle during the event.

Event start (UT)	PRN	Median θ
18 Aug 2022 13:18:00	6	67.5°
18 Aug 2022 13:27:30	6	67.5°
18 Aug 2022 13:49:00	6	67.5°
06 May 2023 11:09:30	9	60°
07 Jul 2023 08:19:43	7	79°
07 Jul 2023 08:52:00	7	79°
07 Jul 2023 08:54:00	7	79°
14 Jul 2023 05:12:52	4	72.5°
02 Aug 2023 13:07:55	6	65°
02 Aug 2023 13:17:20	6	65°

Author contributions. MFI conceived of the study, performed data analysis, and wrote the manuscript. KS analyzed conjunctions, collected data, and developed analysis tools. LS developed analysis tools and provided feedback on the manuscript. DRT performed analysis and provided feedback on the manuscript. PTJ operated GNSS instrumentation and provided feedback on the manuscript. JP-ST, YS, YM, & DRH contributed comments and feedback on the manuscript. MFI, JP-ST, DRH, BP, SM, & GCH operated the ICEBEAR radar and provided data handling; GCH conceived of the radar. SK, KK, YM, TH, AS, KY, AM, YKaz, S-YW, IS, TM, TT, SY, & YKas designed and operated the Arase satellite and provided data handling.

Competing interests. At least one of the (co-)authors is a member of the editorial board of Annales Geophysicae.

Data availability Science data of the ERG (Arase) satellite were obtained from the ERG Science Center operated by ISAS-/JAXA and ISEE/Nagoya University (Miyoshi et al., 2018a)(https://ergsc.isee.nagoya-u.ac.jp/index.shtml.en. This includes Lv.3 HEP (DOI 10.34515/DATA.ERG-01002) version 01_01, Lv.3 MEP-e (DOI 10.34515/DATA.ERG-02003) version 01_01, Lv.2 LEP-e (DOI 10.34515/DATA.ERG-05000) version 04_01, Lv.2 PWE/OFA (DOI 10.34515/DATA.ERG-08000), and Lv.2 MGF (DOI 10.34515/DATA.ERG-06001) version 04_04. SuperMAG data can be accessed at https://supermag.jhuapl.edu/mag/. ICEBEAR 3D echo data for 2020, 2021 is published with DOI 10.5281/zenodo.7509022. CHAIN ISMR data is available at https://chain-new.chain-project.net/index.php/data-products/data-download.

Acknowledgements. This work is supported in part by the European Space Agency's Living Planet Grant No. 1000012348 and by the Research Council of Norway (RCN) Grant No. 324859. We acknowledge the support of the Canadian Space Agency (CSA) [20SUGOICEB], the Canada Foundation for Innovation (CFI) John R. Evans Leaders Fund [32117], the Natural Science and Engineering Research Council (NSERC), the Discovery grants program [RGPIN-2019-19135], the Digital Research Alliance of Canada [RRG-4802].DRT is supported through UK Natural Environment Research Council DRIIVE [NE/W003368/1] and FINESSE [NE/W003147/1] grants. MFI is grateful to J. Park and R. Horne for stimulating discussions. Anthropic's Claude Fable 5 was used to collate information in preparation for the revisions of this manuscript.

References

Baddour, N.: Chapter 1 - Two-Dimensional Fourier Transforms in Polar Coordinates, in: Advances in Imaging and Electron Physics, edited by Hawkes, P. W., vol. 165 of *Imaging and Electron Physics*, pp. 1–45, Elsevier, https://doi.org/10.1016/B978-0-12-385861-0.00001-4, 2011.

Baker, K. B. and Wing, S.: A New Magnetic Coordinate System for Conjugate Studies at High Latitudes, Journal of Geophysical Research: Space Physics, 94, 9139–9143, https://doi.org/10.1029/JA094iA07p09139, 1989.

Barron, J. L., Fleet, D. J., and Beauchemin, S. S.: Performance of Optical Flow Techniques, International Journal of Computer Vision, 12, 43–77, https://doi.org/10.1007/BF01420984, 1994.

Basu, S., Basu, S., MacKenzie, E., Coley, W. R., Sharber, J. R., and Hoegy, W. R.: Plasma Structuring by the Gradient Drift Instability at High Latitudes and Comparison with Velocity Shear Driven Processes, Journal of Geophysical Research: Space Physics, 95, 7799–7818, https://doi.org/10.1029/JA095iA06p07799, 1990.

Blinstrubas, G., English, A., Stuart, D. J., Hampton, D. L., Lamarche, L., Nishimura, Y., and Datta-Barua, S.: Comparative Hypothesis Testing of Auroral Ionospheric Layer Causing Global Navigation Satellite System Scintillation, Space Weather, 23, e2024SW004 069, https://doi.org/10.1029/2024SW004069, 2025.

Boldyrev, S. and Perez, J. C.: SPECTRUM OF KINETIC-ALFVÉN TURBULENCE, The Astrophysical Journal Letters, 758, L44, https://doi.org/10.1088/2041-8205/758/2/L44, 2012.

Bougard, B., Sleewaegen, J.-M., Spogli, L., Veettil, S. V., and Monico, J. F. G.: CIGALA: Challenging the Solar Maximum in Brazil with PolaRxS, in: Proceedings of the 24th International Technical Meeting of the Satellite Division of The Institute of Navigation (ION GNSS 2011), pp. 2572–2579, 2011.

Buneman, O.: Excitation of Field Aligned Sound Waves by Electron Streams, Physical Review Letters, 10, 285–287, https://doi.org/10.1103/PhysRevLett.10.285, 1963.

Chau, J. L. and St.-Maurice, J.-P.: Unusual 5 m E Region Field-Aligned Irregularities Observed from Northern Germany during the Magnetic Storm of 17 March 2015, Journal of Geophysical Research: Space Physics, 121, 10,316–10,340, https://doi.org/10.1002/2016JA023104, 2016.

Chen, L., Wu, D. J., and Huang, J.: Kinetic Alfvén Wave Instability Driven by Field-Aligned Currents in a Low-β Plasma, Journal of Geophysical Research: Space Physics, 118, 2951–2957, https://doi.org/10.1002/jgra.50332, 2013.

Dahlgren, H., Lanchester, B. S., Ivchenko, N., and Whiter, D. K.: Variations in Energy, Flux, and Brightness of Pulsating Aurora Measured at High Time Resolution, Annales Geophysicae, 35, 493–503, https://doi.org/10.5194/angeo-35-493-2017, 2017.

David, V. and Galtier, S.: K_\perp ^-8/3 Spectrum in Kinetic Alfvén Wave Turbulence: Implications for the Solar Wind, The Astrophysical Journal Letters, 880, L10, https://doi.org/10.3847/2041-8213/ab2fe6, 2019.

D'Errico, J.: SLM-shape Language Modeling, SLM-Shape Language Modeling.. http://www. mathworks. com/matlabcentral/fileexchange/24443-slm-shape-language-modeling: Mathworks, 2009.

Dimant, Y. S. and Sudan, R. N.: Kinetic Theory of the Farley-Buneman Instability in the *E* Region of the Ionosphere, Journal of Geophysical Research: Space Physics, 100, 14 605–14 623, https://doi.org/10.1029/95JA00794, 1995.

Drexler, J., St. -Maurice, J.-P., Chen, D., and Moorcroft, D. R.: New Insights from a Nonlocal Generalization of the Farley-Buneman Instability Problem at High Latitudes, Annales Geophysicae, 20, 2003–2025, https://doi.org/10.5194/angeo-20-2003-2002, 2002.

Fang, X., Randall, C. E., Lummerzheim, D., Wang, W., Lu, G., Solomon, S. C., and Frahm, R. A.: Parameterization of Monoenergetic Electron Impact Ionization, Geophysical Research Letters, 37, https://doi.org/10.1029/2010GL045406, 2010.

Farley, D. T.: A Plasma Instability Resulting in Field-Aligned Irregularities in the Ionosphere, Journal of Geophysical Research (1896-1977), 68, 6083–6097, https://doi.org/10.1029/JZ068i022p06083, 1963.

Fejer, B. G. and Kelley, M. C.: Ionospheric Irregularities, Reviews of Geophysics, 18, 401–454, https://doi.org/10.1029/RG018i002p00401, 1980.

Forte, B. and Radicella, S. M.: Problems in Data Treatment for Ionospheric Scintillation Measurements, Radio Science, 37, 8–1–8–5, https://doi.org/10.1029/2001RS002508, 2002.

Foster, J. C. and Erickson, P. J.: Simultaneous Observations of E-region Coherent Backscatter and Electric Field Amplitude at F-region Heights with the Millstone Hill UHF Radar, Geophysical Research Letters, 27, 3177–3180, https://doi.org/10.1029/2000GL000042, 2000.

Fredricks, R. W. and Coroniti, F. V.: Ambiguities in the Deduction of Rest Frame Fluctuation Spectrums from Spectrums Computed in Moving Frames, Journal of Geophysical Research (1896-1977), 81, 5591–5595, https://doi.org/10.1029/JA081i031p05591, 1976.

Friis-Christensen, E., Lühr, H., and Hulot, G.: Swarm: A Constellation to Study the Earth's Magnetic Field, Earth, Planets and Space, 58, BF03351 933, https://doi.org/10.1186/BF03351933, 2006.

Galtier, S. and Meyrand, R.: Entanglement of Helicity and Energy in Kinetic Alfvén Wave/Whistler Turbulence, Journal of Plasma Physics, 81, 325810 106, https://doi.org/10.1017/S0022377814000774, 2015.

Ghidoni, R., Spogli, L., Mevius, M., Cesaroni, C., Alfonsi, L., Beser, K., Guerra, M., and Maestri, T.: Ionospheric Response to the January 2022 Geomagnetic Storm Using LOFAR and GNSS, Journal of Space Weather and Space Climate, 15, 50, https://doi.org/10.1051/swsc/2025052, 2025.

Ghobadi, H., Spogli, L., Alfonsi, L., Cesaroni, C., Cicone, A., Linty, N., Romano, V., and Cafaro, M.: Disentangling Ionospheric Refraction and Diffraction Effects in GNSS Raw Phase through Fast Iterative Filtering Technique, GPS Solutions, 24, 85, https://doi.org/10.1007/s10291-020-01001-1, 2020.

Gillies, D. M., Knudsen, D., Spanswick, E., Donovan, E., Burchill, J., and Patrick, M.: Swarm Observations of Field-Aligned Currents Associated with Pulsating Auroral Patches, Journal of Geophysical Research: Space Physics, 120, 9484–9499, https://doi.org/10.1002/2015JA021416, 2015.

Gillies, D. M., Liang, J., Donovan, E., and Spanswick, E.: The Apparent Motion of STEVE and the Picket Fence Phenomena, Geophysical Research Letters, 47, e2020GL088 980, https://doi.org/10.1029/2020GL088980, 2020.

Hamza, A. M. and St-Maurice, J. P.: A Turbulent Theoretical Framework for the Study of Current-Driven E Region Irregularities at High Latitudes: Basic Derivation and Application to Gradient-Free Situations, Journal of Geophysical Research: Space Physics, 98, 11 587–11 599, https://doi.org/10.1029/92JA02836, 1993.

Hamza, A. M., Song, K., Meziane, K., and Thayyil, J. P.: Two-Component Phase Scintillation Spectra in the Auroral Region: Observations and Model, Preprint, Preprints, https://doi.org/10.22541/essoar.169272227.79637429/v1, 2023.

Hosokawa, K. and Ogawa, Y.: Ionospheric Variation during Pulsating Aurora, Journal of Geophysical Research: Space Physics, 120, 5943–5957, https://doi.org/10.1002/2015JA021401, 2015.

Huba, J. D., Hassam, A. B., Schwartz, I. B., and Keskinen, M. J.: Ionospheric Turbulence: Interchange Instabilities and Chaotic Fluid Behavior, Geophysical Research Letters, 12, 65–68, https://doi.org/10.1029/GL012i001p00065, 1985.

Hultqvist, B. and Egeland, A.: Radio Aurora, Space Science Reviews, 3, 27–78, https://doi.org/10.1007/BF00226644, 1964.

Huyghebaert, D., Hussey, G., Vierinen, J., McWilliams, K., and St-Maurice, J.-P.: ICEBEAR: An All-Digital Bistatic Coded Continuous-Wave Radar for Studies of the E Region of the Ionosphere, Radio Science, 54, 349–364, https://doi.org/10.1029/2018RS006747, 2019.

Ivarsen, M. F.: A Source or a Sink? How the Altitude of Particle Precipitation Influence High-Latitude Electrodynamics, Annales Geophysicae, 44, 149–162, https://doi.org/10.5194/angeo-44-149-2026, 2026.

Ivarsen, M. F., Bull, P., Llinares, C., and Mota, D. F.: Distinguishing Screening Mechanisms with Environment-Dependent Velocity Statistics, Astronomy & Astrophysics, 595, A40, https://doi.org/10.1051/0004-6361/201628604, 2016.

Ivarsen, M. F., Jin, Y., Spicher, A., and Clausen, L. B. N.: Direct Evidence for the Dissipation of Small-Scale Ionospheric Plasma Structures by a Conductive E Region, Journal of Geophysical Research: Space Physics, 124, 2935–2942, https://doi.org/10.1029/2019JA026500, 2019.

Ivarsen, M. F., Park, J., Kwak, Y.-S., Jin, Y., Knudsen, D. J., and Clausen, L. B. N.: Observational Evidence for the Role of Hall Conductance in Alfvén Wave Reflection, Journal of Geophysical Research: Space Physics, 125, e2020JA028 119, https://doi.org/10.1029/2020JA028119, 2020.

Ivarsen, M. F., St-Maurice, J.-P., Jin, Y., Park, J., Miloch, W., Spicher, A., Kwak, Y.-S., and Clausen, L. B. N.: Steepening Plasma Density Spectra in the Ionosphere: The Crucial Role Played by a Strong E-Region, Journal of Geophysical Research: Space Physics, 126, e2021JA029 401, https://doi.org/10.1029/2021JA029401, 2021.

Ivarsen, M. F., Lozinsky, A., St-Maurice, J.-P., Spicher, A., Huyghebaert, D., Hussey, G. C., Galeschuk, D., Pitzel, B., and Vierinen, J.: The Distribution of Small-Scale Irregularities in the E-Region, and Its Tendency to Match the Spectrum of Field-Aligned Current Structures in the F-Region, Journal of Geophysical Research: Space Physics, 128, e2022JA031 233, https://doi.org/10.1029/2022JA031233, 2023a.

Ivarsen, M. F., St-Maurice, J.-P., Hussey, G., Spicher, A., Jin, Y., Lozinsky, A., Goodwin, L. V., Galeschuk, D., Park, J., and Clausen, L. B. N.: Measuring Small-Scale Plasma Irregularities in the High-Latitude E- and F-regions Simultaneously, Scientific Reports, 13, 11 579, https://doi.org/10.1038/s41598-023-38777-4, 2023b.

Ivarsen, M. F., St-Maurice, J.-P., Hussey, G. C., Galeschuk, D., Lozinsky, A., Pitzel, B., and McWilliams, K. A.: An Algorithm to Separate Ionospheric Turbulence Radar Echoes From Those of Meteor Trails in Large Data Sets, Journal of Geophysical Research: Space Physics, 128, e2022JA031 050, https://doi.org/10.1029/2022JA031050, 2023c.

Ivarsen, M. F., Gillies, M. D., Huyghebaert, D. R., St-Maurice, J.-P., Lozinsky, A., Galeschuk, D., Donovan, E., and Hussey, G. C.: Turbulence Embedded Into the Ionosphere by Electromagnetic Waves, Journal of Geophysical Research: Space Physics, 129, e2023JA032 310, https://doi.org/10.1029/2023JA032310, 2024a.

Ivarsen, M. F., Huyghebaert, D. R., Gillies, M. D., St-Maurice, J.-P., Themens, D. R., Oppenheim, M., Gustavsson, B. J., Billett, D., Pitzel, B., Galeschuk, D., Donovan, E., and Hussey, G. C.: Turbulence Around Auroral Arcs, Journal of Geophysical Research: Space Physics, 129, e2023JA032 309, https://doi.org/10.1029/2023JA032309, 2024b.

Ivarsen, M. F., St-Maurice, J.-P., Hussey, G. C., Huyghebaert, D. R., and Gillies, M. D.: Point-Cloud Clustering and Tracking Algorithm for Radar Interferometry, Physical Review E, 110, 045 207, https://doi.org/10.1103/PhysRevE.110.045207, 2024c.

Ivarsen, M. F., St-Maurice, J.-P., Huyghebaert, D. R., Gillies, M. D., Lind, F., Pitzel, B., and Hussey, G. C.: Deriving the Ionospheric Electric Field From the Bulk Motion of Radar Aurora in the E-Region, Journal of Geophysical Research: Space Physics, 129, e2024JA033 060, https://doi.org/10.1029/2024JA033060, 2024d.

Ivarsen, M. F., St-Maurice, J.-P., Jin, Y., Park, J., Buschman, L. M., and Clausen, L. B.: To What Degree Does the High-Energy Aurora Destroy F-region Irregularities?, Frontiers in Astronomy and Space Sciences, 11, https://doi.org/10.3389/fspas.2024.1309136, 2024e.

Ivarsen, M. F., Miyashita, Y., St-Maurice, J.-P., Hussey, G. C., Pitzel, B., Galeschuk, D., Marei, S., Horne, R. B., Kasahara, Y., Matsuda, S., Kasahara, S., Keika, K., Miyoshi, Y., Yamamoto, K., Shinbori, A., Huyghebaert, D. R., Matsuoka, A., Yokota, S., and Tsuchiya, F.: Characteristic E-Region Plasma Signature of Magnetospheric Wave-Particle Interactions, Physical Review Letters, 134, 145 201, https://doi.org/10.1103/PhysRevLett.134.145201, 2025a.

Ivarsen, M. F., St-Maurice, J.-P., Hussey, G. C., Billet, D., Huyghebaert, D. R., Jin, Y., Miyashita, Y., Kasahara, S., Song, K., Jayachandran, P. T., Yokota, S., Miyoshi, Y., Yamamoto, K., Shinbori, A., Kasahara, Y., Shinohara, I., and Matsuoka, A.: Eastward Transients in the Dayside Ionosphere. I. Electrodynamics on Closed Field Lines, Physical Review E, 112, 045 204, https://doi.org/10.1103/r6bv-pzlq, 2025b.

Ivarsen, M. F., St-Maurice, J.-P., Hussey, G. C., McWilliams, K., Jin, Y., Huyghebaert, D. R., Miyashita, Y., and Sibeck, D.: Eastward Transients in the Dayside Ionosphere. II. A Parallel-Plate Capacitorlike Effect, Physical Review E, 112, 045 203, https://doi.org/10.1103/3bzj-bsf8, 2025c.

Ivarsen, M. F., Song, K., St-Maurice, J.-P., and Hussey, G. C.: Excursion-Set Structure Factor of the Auroral Electric Field (in Review at Physical Review Letters), https://doi.org/10.48550/arXiv.2606.26854, 2026.

Jayachandran, P. T., Langley, R. B., MacDougall, J. W., Mushini, S. C., Pokhotelov, D., Hamza, A. M., Mann, I. R., Milling, D. K., Kale, Z. C., Chadwick, R., Kelly, T., Danskin, D. W., and Carrano, C. S.: Canadian High Arctic Ionospheric Network (CHAIN), Radio Science, 44, https://doi.org/10.1029/2008RS004046, 2009.

Jin, Y., Moen, J. I., and Miloch, W. J.: GPS Scintillation Effects Associated with Polar Cap Patches and Substorm Auroral Activity: Direct Comparison, Journal of Space Weather and Space Climate, 4, A23, https://doi.org/10.1051/swsc/2014019, 2014.

Kasahara, S., Yokota, S., Mitani, T., Asamura, K., Hirahara, M., Shibano, Y., and Takashima, T.: Medium-Energy Particle Experiments—Electron Analyzer (MEP-e) for the Exploration of Energization and Radiation in Geospace (ERG) Mission, Earth, Planets and Space, 70, 69, https://doi.org/10.1186/s40623-018-0847-z, 2018.

Kawamura, Y., Hosokawa, K., Nozawa, S., Ogawa, Y., Kawabata, T., Oyama, S.-I., Miyoshi, Y., Kurita, S., and Fujii, R.: Estimation of the Emission Altitude of Pulsating Aurora Using the Five-Wavelength Photometer, Earth, Planets and Space, 72, 96, https://doi.org/10.1186/s40623-020-01229-8, 2020.

Kazama, Y., Wang, B.-J., Wang, S.-Y., Ho, P. T. P., Tam, S. W. Y., Chang, T.-F., Chiang, C.-Y., and Asamura, K.: Low-Energy Particle Experiments–Electron Analyzer (LEPe) Onboard the Arase Spacecraft, Earth, Planets and Space, 69, 165, https://doi.org/10.1186/s40623-017-0748-6, 2017.

Keskinen, M. J.: Nonlinear Stabilization of the Farley-Buneman Instability by Strong E x B Turbulence., Tech. rep., 1981.

Keskinen, M. J. and Huba, J. D.: Nonlinear Evolution of High-Latitude Ionospheric Interchange Instabilities with Scale-Size-Dependent Magnetospheric Coupling, Journal of Geophysical Research: Space Physics, 95, 15 157–15 166, https://doi.org/10.1029/JA095iA09p15157, 1990.

Kintner P. M., Ledvina B. M., and de Paula E. R.: GPS and Ionospheric Scintillations, Space Weather, 5, https://doi.org/10.1029/2006SW000260, 2007.

Kivanc and Heelis, R. A.: Spatial Distribution of Ionospheric Plasma and Field Structures in the High-Latitude F Region, Journal of Geophysical Research, 103, 6955–6968, https://doi.org/10.1029/97JA03237, 1998.

Krämer, E., Koller, F., Suni, J., LaMoury, A. T., Pöppelwerth, A., Glebe, G., Mohammed-Amin, T., Raptis, S., Vuorinen, L., Weiss, S., Xirogiannopoulou, N., Archer, M., Blanco-Cano, X., Gunell, H., Hietala, H., Karlsson, T., Plaschke, F., Preisser, L., Roberts, O., Simon Wedlund, C., Temmer, M., and Vörös, Z.: Jets Downstream of Collisionless Shocks: Recent Discoveries and Challenges, Space Science Reviews, 221, 4, https://doi.org/10.1007/s11214-024-01129-3, 2024.

Lozinsky, A., Hussey, G., McWilliams, K., Huyghebaert, D., and Galeschuk, D.: ICEBEAR-3D: A Low Elevation Imaging Radar Using a Non-Uniform Coplanar Receiver Array for E Region Observations, Radio Science, 57, e2021RS007 358, https://doi.org/10.1029/2021RS007358, 2022.

Marek, M. and Schreiber, R.: Can the Auroral Kilometric Radiation Be a Self-Organized Criticality System?, Earth and Space Science, 9, e2021EA002 148, https://doi.org/10.1029/2021EA002148, 2022.

Marov, M. Y. and Kolesnichenko, A. V.: Self-Organization of Developed Turbulence and Formation Mechanisms of Coherent Structures, in: Turbulence and Self-Organization: Modeling Astrophysical Objects, edited by Marov, M. Y. and Kolesnichenko, A. V., pp. 373–423, Springer, New York, NY, ISBN 978-1-4614-5155-6, https://doi.org/10.1007/978-1-4614-5155-6_6, 2013.

Maynard, N. C., Bahnsen, A., Christophersen, P., Egeland, A., and Lundin, R.: An Example of Anticorrelation of Auroral Particles and Electric Fields, J. Geophys. Res., v. 78, no. 19, pp. 3976-3980, https://doi.org/10.1029/JA078i019p03976, 1973.

McCaffrey, A. M. and Jayachandran, P. T.: Determination of the Refractive Contribution to GPS Phase “Scintillation”, Journal of Geophysical Research: Space Physics, 124, 1454–1469, https://doi.org/10.1029/2018JA025759, 2019.

Meziane, K., Hamza, A. M., and Jayachandran, P. T.: Turbulence Signatures in High-Latitude Ionospheric Scintillation, Journal of Geophysical Research: Space Physics, 128, e2022JA030 934, https://doi.org/10.1029/2022JA030934, 2023.

Meziane, K., Hamza, A. M., Song, K., and Jayachandran, P. T.: Identifying Scales of the Ionospheric Structure Through Scintillation Events, Journal of Geophysical Research: Space Physics, 130, e2025JA034 326, https://doi.org/10.1029/2025JA034326, 2025.

Mitani, T., Takashima, T., Kasahara, S., Miyake, W., and Hirahara, M.: High-Energy Electron Experiments (HEP) Aboard the ERG (Arase) Satellite, Earth, Planets and Space, 70, 77, https://doi.org/10.1186/s40623-018-0853-1, 2018.

Miyoshi, Y., Hori, T., Shoji, M., Teramoto, M., Chang, T. F., Segawa, T., Umemura, N., Matsuda, S., Kurita, S., Keika, K., Miyashita, Y., Seki, K., Tanaka, Y., Nishitani, N., Kasahara, S., Yokota, S., Matsuoka, A., Kasahara, Y., Asamura, K., Takashima, T., and Shinohara, I.: The ERG Science Center, Earth, Planets and Space, 70, 96, https://doi.org/10.1186/s40623-018-0867-8, 2018a.

Miyoshi, Y., Shinohara, I., Takashima, T., Asamura, K., Higashio, N., Mitani, T., Kasahara, S., Yokota, S., Kazama, Y., Wang, S.-Y., Tam, S. W. Y., Ho, P. T. P., Kasahara, Y., Kasaba, Y., Yagitani, S., Matsuoka, A., Kojima, H., Katoh, Y., Shiokawa, K., and Seki, K.: Geospace Exploration Project ERG, Earth, Planets and Space, 70, 101, https://doi.org/10.1186/s40623-018-0862-0, 2018b.

Miyoshi, Y., Shinohara, I., Ukhorskiy, S., Claudepierre, S. G., Mitani, T., Takashima, T., Hori, T., Santolik, O., Kolmasova, I., Matsuda, S., Kasahara, Y., Teramoto, M., Katoh, Y., Hikishima, M., Kojima, H., Kurita, S., Imajo, S., Higashio, N., Kasahara, S., Yokota, S., Asamura, K., Kazama, Y., Wang, S.-Y., Jun, C.-W., Kasaba, Y., Kumamoto, A., Tsuchiya, F., Shoji, M., Nakamura, S., Kitahara, M., Matsuoka, A., Shiokawa, K., Seki, K., Nosé, M., Takahashi, K., Martinez-Calderon, C., Hospodarsky, G., Colpitts, C., Kletzing, C., Wygant, J., Spence, H., Baker, D. N., Reeves, G. D., Blake, J. B., and Lanzerotti, L.: Collaborative Research Activities of the Arase and Van Allen Probes, Space Science Reviews, 218, 38, https://doi.org/10.1007/s11214-022-00885-4, 2022.

Moen, J., Oksavik, K., Alfonsi, L., Daabakk, Y., Romano, V., and Spogli, L.: Space Weather Challenges of the Polar Cap Ionosphere, Journal of Space Weather and Space Climate, 3, A02, https://doi.org/10.1051/swsc/2013025, 2013.

Mounir, H., Berthelier, A., Cerisier, J. C., Lagoutte, D., and Beghin, C.: The Small-Scale Turbulent Structure of the High Latitude Ionosphere - Arcad-Aureol-3 Observations, Annales Geophysicae, 9, 725–737, 1991.

Nishimura, Y., Lessard, M. R., Katoh, Y., Miyoshi, Y., Grono, E., Partamies, N., Sivadas, N., Hosokawa, K., Fukizawa, M., Samara, M., Michell, R. G., Kataoka, R., Sakanoi, T., Whiter, D. K., Oyama, S.-i., Ogawa, Y., and Kurita, S.: Diffuse and Pulsating Aurora, Space Science Reviews, 216, 4, https://doi.org/10.1007/s11214-019-0629-3, 2020.

Oppenheim, M. M. and Dimant, Y. S.: Kinetic Simulations of 3-D Farley-Buneman Turbulence and Anomalous Electron Heating, Journal of Geophysical Research: Space Physics, 118, 1306–1318, https://doi.org/10.1002/jgra.50196, 2013.

Oppenheim, M. M., Dimant, Y., and Dyrud, L. P.: Large-Scale Simulations of 2-D Fully Kinetic Farley-Buneman Turbulence, Annales Geophysicae, 26, 543–553, https://doi.org/10.5194/angeo-26-543-2008, 2008.

Pakhotin, I. P., Mann, I. R., Lysak, R. L., Knudsen, D. J., Gjerloev, J. W., Rae, I. J., Forsyth, C., Murphy, K. R., Miles, D. M., Ozeke, L. G., and Balasis, G.: Diagnosing the Role of Alfvén Waves in Magnetosphere-Ionosphere Coupling: Swarm Observations of Large Amplitude Nonstationary Magnetic Perturbations During an Interval of Northward IMF, Journal of Geophysical Research: Space Physics, 123, 326–340, https://doi.org/10.1002/2017JA024713, 2018.

Palmroth, M., Grandin, M., Sarris, T., Doornbos, E., Tourgaidis, S., Aikio, A., Buchert, S., Clilverd, M. A., Dandouras, I., Heelis, R., Hoffmann, A., Ivchenko, N., Kervalishvili, G., Knudsen, D. J., Kotova, A., Liu, H.-L., Malaspina, D. M., March, G., Marchaudon, A., Marghitu, O., Matsuo, T., Miloch, W. J., Moretto-Jørgensen, T., Mpaloukidis, D., Olsen, N., Papadakis, K., Pfaff, R., Pirnaris, P., Siemes, C., Stolle, C., Suni, J., van den IJssel, J., Verronen, P. T., Visser, P., and Yamauchi, M.: Lower-Thermosphere–Ionosphere (LTI) Quantities: Current Status of Measuring Techniques and Models, Annales Geophysicae, 39, 189–237, https://doi.org/10.5194/angeo-39-189-2021, 2021.

Park, J., Lühr, H., Knudsen, D. J., Burchill, J. K., and Kwak, Y.-S.: Alfvén Waves in the Auroral Region, Their Poynting Flux, and Reflection Coefficient as Estimated from Swarm Observations, Journal of Geophysical Research: Space Physics, 122, 2345–2360, https://doi.org/10.1002/2016JA023527, 2017.

Partamies, N., Whiter, D., Kadokura, A., Kauristie, K., Tyssøy, H. N., Massetti, S., Stauning, P., and Raita, T.: Occurrence and Average Behavior of Pulsating Aurora, Journal of Geophysical Research: Space Physics, 122, 5606–5618, https://doi.org/10.1002/2017JA024039, 2017.

Phelps, A. D. R. and Sagalyn, R. C.: Plasma Density Irregularities in the High-Latitude Top Side Ionosphere, Journal of Geophysical Research, 81, 515–523, https://doi.org/10.1029/JA081i004p00515, 1976.

Prikryl, P., André, D., Sofko, G. J., and Koehler, J. A.: Doppler Radar Observations of Harmonics of Electrostatic Ion Cyclotron Waves in the Auroral Ionosphere, Journal of Geophysical Research: Space Physics, 93, 7409–7424, https://doi.org/10.1029/JA093iA07p07409, 1988.

Prikryl, P., Andre, D., Koehler, J. A., Sofko, G. J., and McKibben, M. J.: Evidence of Highly Localized Auroral Scatterers from 50-MHz CW Radar Interferometry, Planetary and space science, 38, 933–944, 1990.

Redmon, R. J., Denig, W. F., Kilcommons, L. M., and Knipp, D. J.: New DMSP Database of Precipitating Auroral Electrons and Ions, Journal of Geophysical Research: Space Physics, 122, 9056–9067, https://doi.org/10.1002/2016JA023339, 2017.

RGB, T.: UCalgary Space Remote Sensing Group Data Landing Page — UCalgary SRS Data Documentation, 2023.

Robinson, T. R.: Towards a Self-Consistent Non-Linear Theory of Radar Auroral Backscatter, Journal of Atmospheric and Terrestrial Physics, 48, 417–422, https://doi.org/10.1016/0021-9169(86)90118-2, 1986.

Sahr, J. D. and Fejer, B. G.: Auroral Electrojet Plasma Irregularity Theory and Experiment: A Critical Review of Present Understanding and Future Directions, Journal of Geophysical Research: Space Physics, 101, 26 893–26 909, https://doi.org/10.1029/96JA02404, 1996.

Sato, T.: Stabilization of the Two-Stream Instability in the Equatorial Electrojet, Physical Review Letters, 28, 732–734, https://doi.org/10.1103/PhysRevLett.28.732, 1972.

Schlegel, K.: Auroral Zone E-region Conductivities during Solar Minimum Derived from EISCAT Data, Ann. Geophys. (C.N.R.S.); (France), 6:1, 1988.

Shen, Y., Verkhoglyadova, O. P., Artemyev, A., Hartinger, M. D., Angelopoulos, V., Shi, X., and Zou, Y.: Magnetospheric Control of Ionospheric TEC Perturbations via Whistler-Mode and ULF Waves, AGU Advances, 5, e2024AV001 302, https://doi.org/10.1029/2024AV001302, 2024.

Siscoe, G., Raeder, J., and Ridley, A. J.: Transpolar Potential Saturation Models Compared, Journal of Geophysical Research: Space Physics, 109, https://doi.org/10.1029/2003JA010318, 2004.

Song, K., Hamza, A. M., Jayachandran, P. T., Meziane, K., and Kashcheyev, A.: Spectral Characteristics of Phase Fluctuations at High Latitude, Journal of Geophysical Research: Space Physics, 128, e2022JA031 244, https://doi.org/10.1029/2022JA031244, 2023.

Song, K., Meziane, K., Hamza, A. M., and Jayachandran, P. T.: Investigation of the Fresnel Scale From Ionospheric Scintillation Spectra, Journal of Geophysical Research: Space Physics, 130, e2024JA033 239, https://doi.org/10.1029/2024JA033239, 2025.

Spicher, A., Miloch, W. J., and Moen, J. I.: Direct Evidence of Double-Slope Power Spectra in the High-Latitude Ionospheric Plasma, Geophysical Research Letters, 41, 1406–1412, https://doi.org/10.1002/2014GL059214, 2014.

Spogli, L., Ghobadi, H., Cicone, A., Alfonsi, L., Cesaroni, C., Linty, N., Romano, V., and Cafaro, M.: Adaptive Phase Detrending for GNSS Scintillation Detection: A Case Study over Antarctica, IEEE Geoscience and Remote Sensing Letters, 19, 1–5, 2021.

St.-Maurice, J.-P. and Chau, J. L.: A Theoretical Framework for the Changing Spectral Properties of Meter-Scale Farley-Buneman Waves between 90 and 125 Km Altitudes, Journal of Geophysical Research: Space Physics, 121, 10,341–10,366, https://doi.org/10.1002/2016JA023105, 2016.

St-Maurice, J.-P. and Goodwin, L.: Revisiting the Behavior of the E-Region Electron Temperature During Strong Electric Field Events at High Latitudes, Journal of Geophysical Research: Space Physics, 126, 2020JA028 288, https://doi.org/10.1029/2020JA028288, 2021.

St.-Maurice, J.-P. and Hamza, A. M.: A New Nonlinear Approach to the Theory of E Region Irregularities, Journal of Geophysical Research: Space Physics, 106, 1751–1759, https://doi.org/10.1029/2000JA000246, 2001.

St-Maurice, J. P., Kofman, W., and Kluzek, E.: Electron Heating by Plasma Waves in the High Latitude E-region and Related Effects: Observations, Advances in Space Research, 10, 225–237, https://doi.org/10.1016/0273-1177(90)90256-Y, 1990.

St-Maurice, J.-P., Huyghebaert, D., Ivarsen, M. F., and Hussey, G. C.: Narrow Width Farley-Buneman Spectra Above 100 Km Altitude, Journal of Geophysical Research: Space Physics, 128, e2022JA031 191, https://doi.org/10.1029/2022JA031191, 2023.

Sudan, R. N. and Keskinen, M.: Theory of Strongly Turbulent Two-Dimensional Convection of Low-Pressure Plasma, Physical Review Letters, 38, 966–970, https://doi.org/10.1103/PhysRevLett.38.966, 1977.

Sudan, R. N., Akinrimisi, J., and Farley, D. T.: Generation of Small-Scale Irregularities in the Equatorial Electrojet, Journal of Geophysical Research (1896-1977), 78, 240–248, https://doi.org/10.1029/JA078i001p00240, 1973.

Tesema, F., Partamies, N., Nesse Tyssøy, H., and McKay, D.: Observations of Precipitation Energies during Different Types of Pulsating Aurora, Annales Geophysicae, 38, 1191–1202, https://doi.org/10.5194/angeo-38-1191-2020, 2020.

Teunissen, P. J. and Montenbruck, O., eds.: Springer Handbook of Global Navigation Satellite Systems, Springer International Publishing, Cham, ISBN 978-3-319-42926-7 978-3-319-42928-1, https://doi.org/10.1007/978-3-319-42928-1, 2017.

Themens, D. R., Jayachandran, P. T., Galkin, I., and Hall, C.: The Empirical Canadian High Arctic Ionospheric Model (E-CHAIM): NmF2 and hmF2, Journal of Geophysical Research: Space Physics, 122, 9015–9031, https://doi.org/10.1002/2017JA024398, 2017.

Tsunoda, R. T.: High-Latitude F Region Irregularities: A Review and Synthesis, Reviews of Geophysics, 26, 719–760, https://doi.org/10.1029/RG026i004p00719, 1988.

Tsunoda, R. T., Livingston, R. C., McClure, J. P., and Hanson, W. B.: Equatorial Plasma Bubbles: Vertically Elongated Wedges from the Bottomside F Layer, Journal of Geophysical Research: Space Physics, 87, 9171–9180, https://doi.org/10.1029/JA087iA11p09171, 1982.

Tsyganenko, N. A. and Sitnov, M. I.: Modeling the Dynamics of the Inner Magnetosphere during Strong Geomagnetic Storms, Journal of Geophysical Research: Space Physics, 110, 2004JA010 798, https://doi.org/10.1029/2004JA010798, 2005.

Vickrey, J. F. and Kelley, M. C.: The Effects of a Conducting E Layer on Classical F Region Cross-Field Plasma Diffusion, Journal of Geophysical Research: Space Physics, 87, 4461–4468, https://doi.org/10.1029/JA087iA06p04461, 1982.

Villain, J. P., Hanuise, C., and Beghin, C.: ARCAD3-SAFARI Coordinated Study of Auroral and Polar F-region Ionospheric Irregularities, Annales Geophysicae, 4, 61–68, 1986.

Wood, A. G., Alfonsi, L., Clausen, L. B. N., Jin, Y., Spogli, L., Urbář, J., Rawlings, J. T., Whittaker, I. C., Dorrian, G. D., Høeg, P., Kotova, D., Cesaroni, C., Cicone, A., Miedzik, J., Gierlach, E., Kochańska, P., Wojtkiewicz, P., Shahtahmassebi, G., and Miloch, W. J.: Variability of Ionospheric Plasma: Results from the ESA Swarm Mission, Space Science Reviews, 218, 52, https://doi.org/10.1007/s11214-022-00916-0, 2022.

Yeh, K. C. and Liu, C.-H.: Radio Wave Scintillations in the Ionosphere, IEEE Proceedings, 70, 324–360, 1982.

Zhang, Y. and Varney, R. H.: A Statistical Survey of E-Region Anomalous Electron Heating Using Poker Flat Incoherent Scatter Radar Observations, Journal of Geophysical Research: Space Physics, 129, e2023JA032 360, https://doi.org/10.1029/2023JA032360, 2024.